The Squeezing of Eddies through Gaps

HARPER LIGHTFOOT SIMMONS AND DORON NOF*

Department of Oceanography, The Florida State University, Tallahassee, Florida

(Manuscript received 31 July 2000, in final form 29 June 2001)

ABSTRACT

The islands of the Lesser Antilles present a porous meridional barrier to North Brazil Current (NBC) rings. To better understand if, when, and how a NBC ring could be squeezed into the Caribbean Sea through such a gappy barrier, the encounter of a westward drifting eddy with a porous meridional wall is considered. First an eddy encountering a single aperture is modeled. To do so, both an analytical model and a reduced-gravity primitive equations numerical model are used. This was followed by numerical experiments that explored eddy collisions with barriers containing many gaps. In all of these models, the collisions were forced by either β or a steady advection through the gap(s).

Using integrated constraints, an analytical solution was constructed for a zero potential vorticity lens passing through a single gap on a β plane. The solution involves a small parameter ε, the ratio of the short timescale associated with the f-plane adjustment, and the long encounter timescale due to β. It is found that, throughout the encounter, the lens remains axisymmetric and is drained by wall jets. Ultimately, the lens diameter adapts to the gap width so that the eddy loses contact with the walls and drifts slowly into the interior of the western basin. Numerical simulations are in good agreement with this theory.

Numerical experiments also revealed that, just like a lens forced by β, an *intense* advected lens remained axisymmetric as it was slowly drained by wall jets. These intense lenses were ''stiff'' in the sense that they were not distorted by the strain resulting from the convergence of the advecting flow as it passed through the gap. Because of the stiffness of the eddy, it ''stalled'' and traveled through the gap more slowly than the underlying fluid. By contrast, weak lenses were ''slaves'' in the sense that they were squeezed through the gap with the advecting flow. No wall jets were present in this weak lens case.

Numerical simulations of the analogous multiple gap problem revealed that, in contrast to most of the single gap problems, *all* the fluid from the approaching eddy penetrated into the interior of the western basin. This was true for both β and advection. Circulation (accounted for by nonlinear flow separations) developed around the individual islands. When the individual islands were small compared to the eddy (e.g., $L/R_i = 0.3$, where R_i is the initial radius of the lens and L is the island scale), the lens reformed in the lee of the gaps and thus entered the western basin as a single, albeit weakened, vortex. Lenses exhibited signs of breaking when they encountered islands of intermediate size (e.g., $L/R_i = 0.5$). The presence of β greatly enhanced the tendency of the eddy to break in this particular case. Eddies that encountered large islands (e.g., $L/R_i = 1.5$) due to either β or advection almost always broke up into a number of smaller offspring.

Many of the islands of the Lesser Antilles (LA) have spatial scales of $L/R_i = 0.5$ (assuming a ''typical'' NBC radius of 150 km), but there are also some larger obstructions (such as the Grenadines) that are closer to $L/R_i = 1.5$. Since both β and advection are present in the ocean, these single and multiple gap experiments suggest that the NBC rings/LA collision is in a sensitive regime where NBC rings are often, but not always, shattered as they are forced to squeeze through the passages. Counter-intuitively, smaller, more intense NBC rings are broken up by the islands of the LA, whereas larger and weaker eddies are pushed into the Caribbean Sea as coherent structures, particularly if they collide with the relatively smaller islands to the north of the Grenadines.

1. Introduction

The equatorial currents of the western tropical Atlantic have been the subject of several recent reviews (Schott et al. 1998; Schmitz 1996). The summer and fall circulation is dominated by the retroflection of the North Brazil Current (NBC), which carries about 30 to 50 Sverdrups (Sv $\equiv 10^6$ m^3 s^{-1}) of surface water to the east as the North Equatorial Countercurrent (Brown et al. 1992). The observations of Johns et al. (1990), Didden and Schott (1993), Richardson et al. (1994), and Fratantoni et al. (1995) suggest that the NBC retroflection sheds at least three rings per year. These rings are observed to migrate along the South American coast toward the Lesser Antilles (LA), a densely packed island arc that obstructs the entrance to the Caribbean Sea (see

* Additional affiliation: Geophysical Fluid Dynamics Institute, The Florida State University, Tallahassee, Florida.

Corresponding author address: Dr. Harper L. Simmons, School of Earth and Ocean Sciences, University of Victoria, Box 3055, Victoria, BC V8W 3P6 Canada.
E-mail: harper@ocean.seos.uvic.ca

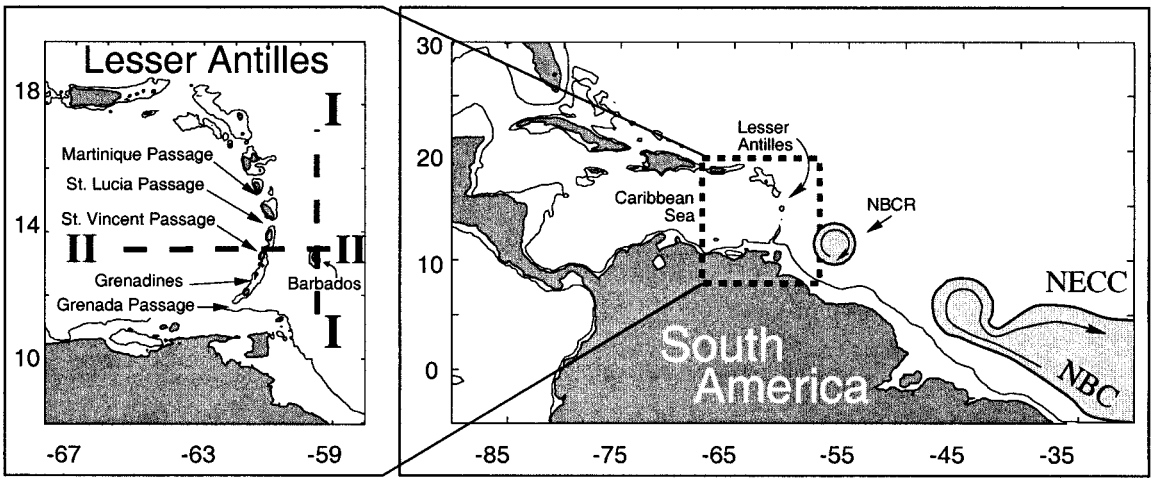

FIG. 1. Schematic diagram (right panel) of the region of interest, indicating the North Brazil Current (NBC) retroflecting to form the North Equatorial Countercurrent (NECC), and a North Brazil Current ring (NBCR) in the vicinity of the Lesser Antilles [adapted from Richardson (1994)]. A second NBCR is in the process of being pinched off from the retroflecting NBC. Note that, due to the variation of the Coriolis parameter with latitude, the radius of a NBCR decreases as it translates meridionally from the NBC retroflection to the Lesser Antilles. (Left) Detail of the Lesser Antilles region (left panel). Cross sections I-I and II-II are shown in Fig. 2. (The passage names follow the National Geographic convention of naming the passages by the island immediately to the north; inconsistent naming has penetrated into some previous author's articles.) The 200-m isobath is indicated in both panels.

Figs. 1 and 2). Based on an estimated meridional transport of 1 Sv per ring (e.g., Fratantoni et al. 1995), a lower bound of 3 Sv [20% of the total upper-ocean cross-gyre transport required by the Atlantic thermohaline overturning (Rintoul 1991)] is attributed to the eddy meridional migration. More recent estimates suggest that as many as four to six NBC rings (NBCRs) per year are shed annually (Pauluhn and Chao 1999; Barnier et al. 2001; Goni and Johns 2001), making the fate of NBCRs even more pertinent.

Although rings and eddies are in general not thought to be an important component of the meridional oceanic heat flux (see, e.g., Olson 1991), NBCRs constitute a crucial link in the thermohaline and conveyor circulation. In this context, it is important to determine to what degree the LA constitutes a barrier to the At-

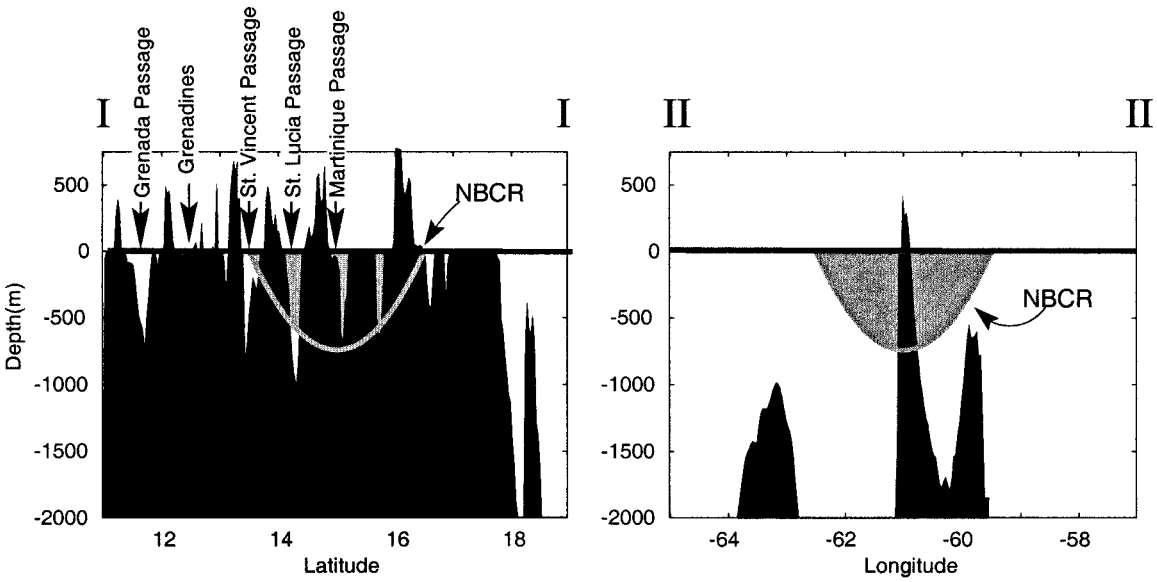

FIG. 2. Meridional cross section (left) of the Lesser Antilles from the point of view of a ''typical'' NBCR approaching the Lesser Antilles from the east. The ring is a ''hypothetical'' ring superimposed on the topography to illustrate the scales. The location of the section is marked by I-I in Fig. 1. A zonal cross section (right) through the St. Vincent Passage, looking north to St. Vincent Island. The location of this cross section is marked by II-II in Fig. 1. Note that many of the passages of the LA are of a much smaller lateral scale than the rings and that the islands appear as nearly vertical walls. [One-thirtieth-degree topography data from the dataset of Smith and Sandwell (1997).]

TABLE 1. Transport estimates (in Sv) of water warmer than 24°C (thought to be of South Atlantic origin). The position of the passages is shown in Fig. 2.

	Passage			
Study	Grenada	St. Vincent	St. Lucia	Total
SR91	2.2	1.5	0.8	4.5
WJ97	2.8	2.3	0.8	5.9

lantic meridional overturning cell. To do so, we shall first present a numerical simulation of an eddy forced by β through a boundary containing a single gap. The results of this experiment will motivate an analytical solution. We will then use our numerical model to complement the theory and examine this process in detail. Further numerical experiments will address a lens advected by a mean flow through a single gap. With this information in hand we shall then investigate the effects of β and advection on lenses forced through barriers containing many gaps.

a. Observational background

1) NORTH BRAZIL CURRENT RINGS

As is the case with most rings resulting from retroflecting currents, NBCRs are larger than rings resulting from instability (e.g., Gulf Stream or Kuroshio rings). They have a diameter of approximately 200–400 km, a depth of 400–600 m, and a migration rate of 10–15 cm s^{-1} along the coast of South America.

Recent estimates of the transport in the passages of the LA have been given by Wilson and Johns (1997) and Johns et al. (1999). According to Schmitz and Richardson (1991), the Florida Current comprises 4.5 Sv of relatively fresh, warm surface waters of South Atlantic origin (>24°) that have passed through the southern Caribbean Sea passages (the Grenada, St. Vincent, and St. Lucia passages indicated in Fig. 1). Using the same temperature classification, Wilson and Johns (1997) estimated that 5.9 Sv of warm, fresh surface waters of South Atlantic origin enter the Caribbean Sea through the southern passages of the LA (Table 1). The lower bound of 3 Sv of intergyre transport attributed to NBCRs thus represents a significant fraction of the total transport through the passages.

Many authors report eddies of NBC origin to the east of the Lesser Antilles (e.g., Didden and Schott 1993; Richardson et al. 1994; Fratantoni et al. 1995; Limeburner et al. 1995; Stansfield et al. 1995). It is clear from some drifter trajectories (Limeburner et al. 1995) that at least a fraction of the rings does enter the Caribbean Sea (Fig. 3). For instance, all drifters of Limeburner et al. (1995) entrained in NBCRs either entered the Caribbean Sea or ''beached'' on the LA.

There is also some evidence for NBCR penetration into the Caribbean Sea from satellite altimetry data. Comparing spectral estimates from TOPEX/Poseidon (T/P) sea surface height anomaly data at the NBC retroflection to spectral estimates obtained from T/P and tide gauges inside the Caribbean Sea, Pauluhn and Chao (1999) inferred that the observed sea surface height variability in the Caribbean Sea is due to anticyclonic eddies generated in the NBC retroflection area. Goni and Johns (2001) used T/P data to track 40 NBCRs in the period 1992–98. During that time, they were able to follow five NBCRs from their formation at the NBC retroflection, through the LA, and into the Caribbean Sea.

Simmons (2000) used T/P data to identify a North

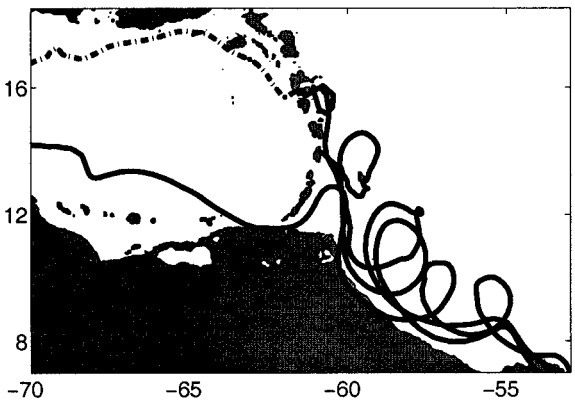

FIG. 3. The tracks of three drifters (originating from the Amazon River outflow) entrained into North Brazil Current rings. As a result of the Lesser Antilles island chain, the drifters are either carried into the Caribbean by the eddies, or ''beach'' themselves due to encounters with topography. The dashed track indicates that the drifter has lost its drogue. [Adapted from Limeburner et al. (1995).] All topography above the 200-m isobath is shaded gray.

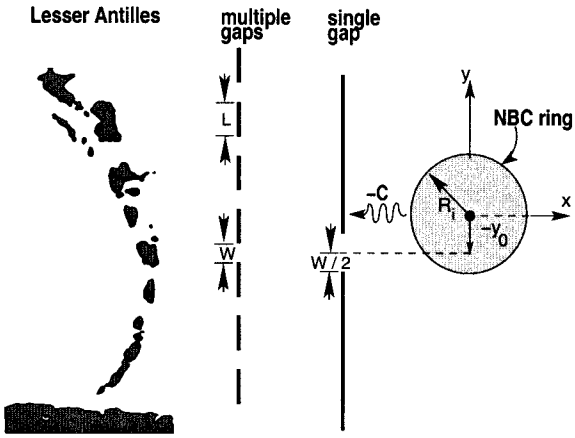

FIG. 4. Two simplifications of the eddy–Antilles problem. Initially the encounter of an eddy with a single gap; We then the island chain taken to be a meridional wall with multiple gaps. The gap width is W, the initial eddy diameter is R_i, and the island length is L. The offset parameter, y_0, measures the shift of the lens center in the y direction relative to the gap. For the single gap studies y_0 will always be zero. The wiggly arrow indicates the propagation of the eddy. The islands of the Lesser Antilles, as delineated by the 200-m isobath, are drawn to scale on the left; the eddy is 300 km in diameter.

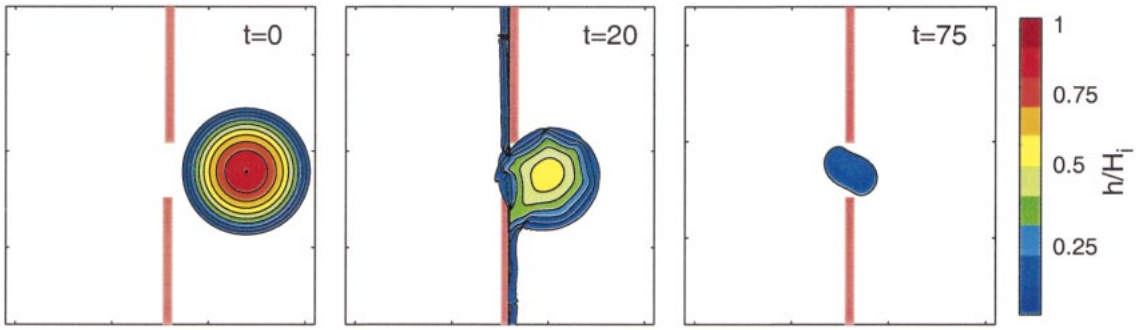

FIG. 5. Snapshots of nondimensional layer thickness from a single gap numerical experiment using β as a propulsion mechanism. The time in days is indicated in each panel. The salient features of this preliminary experiment are that the lens is forced through the gap much more slowly than the adjustment timescale ($1/f$), it remains nearly axisymmetric, and is slowly drained via symmetric wall jets.

Brazil Current Ring ''corridor'' that extends from the NBC retroflection, through the LA, and into the Caribbean Sea. He tracked six NBCRs along this corridor over a 5½-year period. He also showed that these NBCRs ''stall'' at the entrance to the LA and slip to the north of Barbados before entering the Caribbean Sea at 15.5°N. We shall see later that this stalling effect is also reflected in our modeling studies. For other issues related to NBCRs, the reader is referred to Cochrane et al. (1979), Bruce (1984), Bruce and Kerling (1984), and Bruce et al. (1985).

2) CARIBBEAN SEA EDDIES

The eastern Caribbean Sea is a region of large eddy activity. Altimetric observations show that the Caribbean Sea is a region of high variability (see, e.g., Carton and Chao 1999; Simmons 2000). Molinari et al. (1981) reported on three surface drifters entrained in an anticyclonic eddy just west of the LA. The drifters looped in a 60-km radius a total of 5.5 times with a swirl speed of 90 cm s^{-1}. Heburn et al. (1982) attributed these eddies to instability of the westward flow within the Caribbean Sea. They believed that these features were too large (about 100 km) to have come through the passages (less than 40 km), and therefore must have formed locally. Our own study will later suggest that *no rings are too large* to enter the Caribbean Sea from the east. In other words, we will show that even passages as narrow as the LA do not necessarily constitute a barrier to NBCRs and that the large eddy variability observed in the eastern Caribbean Sea may at least in part be due to the penetration of NBCRs from the east.

b. Theoretical and numerical modeling background

There have been no previous theoretical or numerical studies of the eddy–gap problem. Selected OGCM experiments [e.g., Murphy et al. (1999) and Barnier et al. (2001), who used a ¼° model, and Carton and Chao (1999), who used ⅓° model] found that the potential vorticity anomaly of the NBC rings passed directly into the Caribbean Sea with little response to the topography of their modeled LA. In these models, the grid scale was of the same order as the passage widths, so their gaps were only resolved by one or two grid points and their LA were represented by only a few islands. Passages whose widths are close to the grid scale will be governed primarily by viscous dynamics, which suppresses inertial dynamics (McWilliams 1998). This makes the interpretation of such runs difficult. All of these models generate NBC rings, but show different pathways into the Caribbean Sea.

The general eddy–gap problem involves both a response to a narrow passage and a response to a shoaling bottom. We shall neglect the effect of a shoaling bottom in our study; the interested reader is referred to discussions of an eddy's response to bottom topography by Firing and Beardsley (1976), Louis et al. (1982), Smith and O'Brien (1983), Mory et al. (1987), Carnevale et al. (1991), Swaters and Flierl (1991), Velasco Fuentes and van Heijst (1994), Kamenkovich et al. (1996), and LaCasce (1998). The reader is also referred to the following studies of mean flow over a chain of seamounts: Davies (1972), Hogg (1973), McCartney (1975), Huppert and Bryan (1976), Boyer and Davies (1982), and Haidvogel et al. (1993). Relevant laboratory work has been reported by Zhang and Boyer (1991) and Sanson et al. (1998).

Ruddick (1987) analytically established a criterion for the existence of a steady solution for a lens in a simple strain similar to that produced by an advective flow through a gap. He found that, surprisingly, even small strain in the surrounding fluid [$O(10^{-1} f)$] was sufficient to preclude the existence of a steady zero potential vorticity (PV) lens (whose relative vorticity is $-f$). We shall see that some of this tendency will be present in our numerical simulations. Nof (1999) presented an analytical solution for the draining (and eventual decay) of an intensely nonlinear lens forced by β into a solid western boundary without gaps. His solution is associated with a three-way balance between the Coriolis force (due to the slow migration of the lens center toward the wall), the β force (due to the differential Cor-

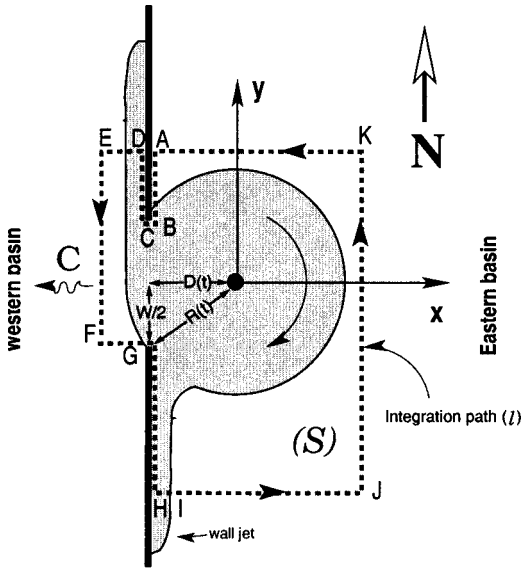

FIG. 6. Schematic diagram of an eddy forced through a meridional western boundary containing a single gap. Initially, the lenslike eddy drifts freely to the west. When it reaches the gap, it begins to leak fluid to the north and south via wall jets. As it leaks, it slowly shrinks and its westward migration rate gradually decreases. Its center ultimately reaches the center of the gap (at which point its diameter becomes identical to the gap width). At this point the lens loses contact with the gap. The integration path (l) that will be used to analyze this process is indicated by **A**–**B**–**C**–**D**–**E**–**F**–**G**–**H**–**I**–**J**–**K**–**A**, and the area bounded by this path is S. The variables $D(t)$, W, and $R(t)$ refer, respectively, to the distance of the lens center to the wall, the gap width, and the lens radius. The wiggly arrows refer to the propagation of the feature (and the coordinate system origin) at a speed $C = dD/dt$.

iolis force experienced by a particle during the northern and southern component of its orbit around the lens), and the rocket force (resulting from fluid draining from the lens as a wall jet). The analytical component of the present paper closely parallels the Nof (1999) solution, which is a direct antecedent to this work.

c. Definition of the problem

Consider again Figs. 1 and 2. The islands appear to be like a picket fence with gap widths that are 10%–20% of the diameter of a typical NBCR. It would thus seem more likely that a camel could pass through the eye of a needle than a NBC ring of 200–300 km diameter could pass through the 30 km gaps of the LA. We wish to determine whether or not these islands and narrow gaps constitute an impenetrable barrier to the passage of NBCRs. Topographic effects due to the shallow sill depths may be important but, as mentioned, they are not addressed on the grounds that the topographic slope is much greater than the ring interface slope so that effectively the rings ''see'' a vertical wall (Fig. 2). Likewise, the issue of hydraulic control is not addressed because with typical values of $U \sim 50$ cm s^{-1} and $H \sim 500$ m (Wilson and Johns 1997), the Froude number is considerably less than unity.

We believe that it is best to break up the problem into two subproblems, conceptually illustrated in Fig. 4. First, we shall look at anticyclones squeezed through a single gap in a thin vertical wall of infinite north–south extent. As a second step, we shall examine the collision of an anticyclone with a western boundary that comprises multiple gaps and islands.

The main questions that we wish to address are 1) what determines the size of rings that can be forced into the Caribbean Sea 2) what controls the fragmentation process—the passage width to eddy size ratio or the island to eddy-size ratio—and 3) lastly and probably most importantly, to what degree do the LA act as a barrier to this leg of the meridional overturning circulation?

d. Approach

We consider lenses with the structure

$$h,\ v_\theta = \begin{cases} H_i - \dfrac{f_0^2 r^2}{8g'}(2 - \mathrm{Ro})\mathrm{Ro}, \qquad -\dfrac{1}{2}\mathrm{Ro} f_0 r & \text{when } r \le 2\left[\dfrac{2}{2(2-\mathrm{Ro})}\right]^{1/2} R_d \\ 0 & \text{when } r > 2\left[\dfrac{2}{2(2-\mathrm{Ro})}\right]^{1/2} R_d, \end{cases} \tag{1}$$

where most of the notation is conventional, that is, the initial central thickness of the eddy is H_i, the lens Rossby number, Ro, is defined so that Ro = 1 corresponds to a zero PV lens, and $R_d = (g'H_i)^{1/2}/f$ is the initial Rossby radius (based on H_i). Hereafter, the subscript i will be used to denote quantities associated with the initial lens. For clarity all variables are defined in both the text and in the appendix. We wish to emphasize that our lens is a *compact* structure whose layer depth vanishes at its boundary.

We shall first consider a lenslike eddy forced by β through a single aperture in an infinitely long meridional wall (section 2). We adopt the plausible assumption that the lens is exactly aligned with the gap center

(i.e., $y_0 = 0$ in Fig. 4). This assumption is justified because even a miniscule advection through the gap [which is certainly present in gaps of the LA: see, e.g., Schmitz and Richardson (1991) or Wilson and Johns (1997)] will center the lens. A collision that is entirely poleward of the gap results in a different set of problems involving jet–gap dynamics and the lens–wall collisions addressed by Nof (1999); it is not of interest here. Similarly, when the collision is south of the gap, the problem is a pure lens–wall collision, as considered by Nof (1999).

We will begin our discussion by reporting on a numerical experiment that will illustrate many of the processes at work and serve to motivate the assumptions required to determine an analytical solution. The experiment was conducted using a finite difference (C grid), primitive equation, reduced-gravity numerical model [derived from that of Bleck and Boudra (1986)] that integrates the fully nonlinear reduced-gravity equations (with $C \equiv 0$, and the introduction of Laplacian friction). This type of model is especially well suited to studies of lenses because of its flux-corrected transport advection algorithm (Zalesak 1979) that performs well in regions of vanishing layer thickness (present along the boundary of a lens). Consistent with the inviscid analytical model, the boundary condition along the wall was free slip. Open boundary conditions of the Orlanski (1976) type were used to permit fluid to leave the computational domain where necessary without noticeably disturbing the outgoing flow.

We initialized the upper layer using (1) and allowed the lens to drift due westward for several days before striking the gap. Its initial westward drift rate is very nearly $-\beta R^2/12$, as predicted by the theory of Nof (1981). The subsequent evolution of the lens is illustrated in Fig. 5. We find that as the lens is forced through the gap, the flow circulating along the rim stagnates and splits into two wall jets that leak fluid along the eastern side of the southern wall and the western side of the northern wall (Fig. 6). Over a period of about 75 days, the lens slowly shrinks as it loses mass to the wall jets. Finally, it is so reduced that it loses contact with the walls and drifts freely into the western basin. Throughout the encounter, the lens remains surprisingly axisymmetric.

Based on this numerical experiment, and following Nof (1999), we will consider the problem to be a slowly varying process. The fast timescale associated with the f-plane adjustment of the lens is $O(f^{-1})$ (the time required for a particle within the lens to complete a revolution), whereas the slow timescale is $O(\beta R_i)^{-1}$ (the time that it takes the lens to pass through the gap). The small parameter, $\varepsilon = \beta R_i/f$, measures the ratio of the two timescales.

We shall analyze the integrated balance of forces acting on the lens in a coordinate system attached to the zonally translating center of the lens. We have observed from our initial numerical experiment that the jets are symmetrical. We shall see that this symmetry results in a balance between the Coriolis and the β forces. This force balance is identical to the open ocean balance, with the critical difference that the lens radius (and, hence, its migration rate through the gap) is now a function of time (or equivalently, the position of the lens relative to the gap). As the lens migrates through the gap, it slowly shrinks until its diameter becomes identical to the gap width and its center is aligned with the axis of the wall, at which point the encounter is complete.

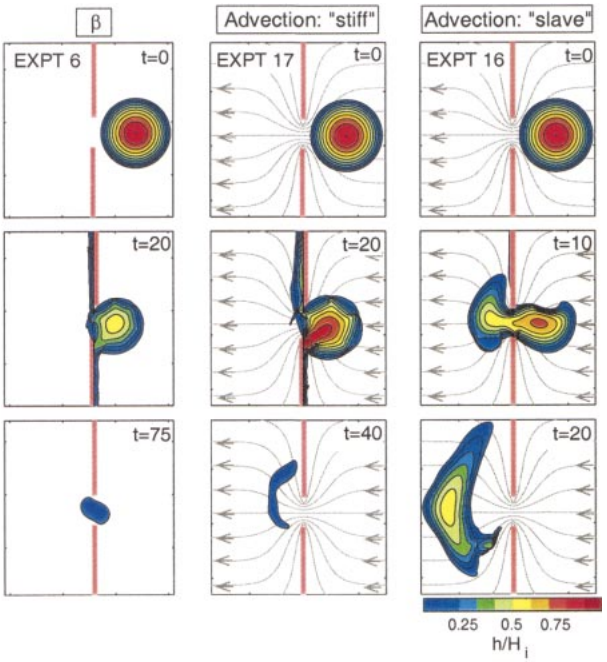

FIG. 7. Snapshots of nondimensional layer thickness from typical single gap numerical experiments. The time in days is indicated in each panel, and the color bar on the lower right applies to all nine panels. A typical experiment (expt 6) using β as a propulsion mechanism (left). As the lens moves through the gap, it remains axisymmetric and is slowly drained via two wall jets. At the final stage (day 75), the lens retains less than 1% of its initial volume and energy. A numerical experiment (expt 17) illustrating the advection of an intense lens through a narrow gap (center). The light lines show the streamlines of the advective flow. The lens is stiff and stalls in front of the gap while the underlying fluids slips through. At the final stage (day 40), the lens retains less than 1% of its initial volume and energy. A numerical experiment (expt 16) illustrating the advection of a weak lens through a narrow gap (right). This lens is clearly a slave to the advection and is forced through the gap with negligible interaction with the wall. At the final stage (day 20), the lens retains 85% of its initial volume and 53% of its initial energy. Notice that although the advection and gap width are the same for both the slave and stiff experiments, the slave lens is drawn through the gap in 20 days, whereas the stiff lens is drawn through in 40 days.

For a lens that is advected through a gap by fluid moving around and below it, we can define a new small parameter, μ, (analogous to our definition of ε) as the ratio of the speed of the advecting flow through the center of the gap (denoted U) to the swirl speed of the lens [i.e., $\mu = U/(f\mathrm{Ro}R_i)$]. Numerical experiments (sec-

tion 3) will reveal that the outcome of advection-induced collisions of an *intense* lens (Ro = 1) are very similar to those of the β-induced collision. In this case, the lens is ''stiff'' in the sense that it is not sheared by the strain present in the advective flow. The stiffness of the lens causes it to stall in front of the gap while the advecting fluid slips underneath and around the lens and into the adjoining basin. It remains axisymmetric and slowly migrates into the gap as it shrinks due to the slow drainage of fluid via symmetric wall jets.

On the other hand, we shall see that when the lens is weak (Ro = 1/4) and the advection is strong ($\mu > 0.3$), the lens is severely distorted as it is squeezed through the gap. In this case, the fluid is prevented from coming into contact with the walls by the convergent lower layer flow, and hence does not drain via wall jets. Thus, the lens fluid is a ''slave'' to the lower layer flow and the volume of lens fluid driven into the western basin by the advecting lower layer is equal to the initial volume.

Numerical simulations of an eddy's collisions with a boundary comprising multiple gaps (section 4) will reveal that all of the fluid from the lens ultimately penetrates into the western basin leaving negligible amounts of fluid trapped by the walls. We shall see that when the spacing between the gaps (which is related to the island length) is small relative to the initial eddy radius, the lens passes through numerous passages but reforms into a single coherent structure in the adjoining basin. We shall also see that, when the spacing between the gaps is large, the eddy breaks up into a number of smaller offspring. The final state of the lens is sensitive to a number of parameters including the gap spacing β, the lens intensity, and the resting layer depth.

2. Single gap theory

We now present our analytical solution for a zero PV lens forced by β through a single gap. Before we begin, it is important to stress that, due to the complicated nature of the governing equations and the fact that there are wall jets, it is very difficult to simply nondimensionalize and commence with a regular perturbation analysis. The approach will therefore be to keep the equations in a dimensional form and argue the relative importance of each term on physical grounds. Much of our analysis parallels Nof (1999), to which the reader who wishes for excruciating detail regarding the scalings is referred.

It is useful to a priori introduce the governing equations that we seek. The first is the straightforward integrated continuity equation

$$\frac{d}{dt}\iint h\, d\mathcal{S} = q,$$

where q is the mass flux out of the eddy carried by the two wall jets. The second is the not-so-obvious momentum-flux equation,

$$C(t)\iint_{\mathcal{S}} fh(t)\, d\mathcal{S} + \beta\iint_{\mathcal{S}} \psi(t)\, d\mathcal{S} = 0,$$

which is a (slowly varying) balance between the northward Coriolis force (associated with the gradually decreasing westward drift of the lens), and the gradually decreasing southward β force. Here, there are no terms for the forces arising from the wall jets because they are assumed to be symmetric so that their flow forces cancel each other. [With this presentation of the final equations, the reader primarily interested in the results can go directly to (10)–(17).]

a. Derivation of the governing equations

The vertically integrated continuity and y-momentum equation are

$$\frac{\partial h}{\partial t} + \frac{\partial}{\partial x}(hu) + \frac{\partial}{\partial y}(hv) = 0 \quad \text{and} \tag{2}$$

$$h\frac{\partial v}{\partial t} + hu\frac{\partial v}{\partial x} + hv\frac{\partial v}{\partial y} + (f_0 + \beta y)(u + C)h = -\frac{g'}{2}\frac{\partial}{\partial y}h^2, \tag{3}$$

where the coordinate system is traveling in the positive x direction at a speed $C(t)$. Equations (2) and (3) comprise terms of three different *relative* magnitudes. They contain terms that we shall refer to as ''large'' [i.e., $O(1)$], ''small'' [i.e., $O(\varepsilon)$], and ''very small'' [i.e., $O(\varepsilon^{3/2})$ or higher]. In what follows, the large terms will drop out due to an area integration. We shall, therefore, keep both large and small terms but neglect the *very* small terms. It can be immediately seen that the term containing the time derivative in (3) is very small and can be neglected because both C and the time-dependent perturbations in u and v are small and t is the *long* timescale. Note, however, that (2) remains unaltered because $\partial h/\partial t$ is ''small'' but not ''very small.''

1) Integrated continuity

The conservation of lens mass is

$$-\frac{d}{dt}\iint_{\mathcal{S}} h\, d\mathcal{S} = \frac{g'(h_H^2 + h_D^2)}{2f_0}, \tag{4}$$

where h_H and h_D are the thicknesses of the jets along the southern and northern walls, respectively (see Fig. 6). Equation (4) states that the mass flux out of the eddy equals the geostrophic transport in the wall jets. Because the volume scales as $g'H_i^2 f^{-2}$ and its variation is on the slow timescale [$t \sim O(\varepsilon^{-1}f^{-1})$], h_H and h_D are $O(\varepsilon^{1/2}H_i)$.

2) Integrated momentum

We can now proceed to consider the integrated x-momentum balance (obtained from the integrated y-mo-

mentum equation). Integrating (3), with the time-dependent term neglected, over the area $\mathcal{S}$ indicated in Fig. 6, and making use of the continuity equation (with $\partial h/\partial t$ intact), we obtain

$$\int\int_{\mathcal{S}}\left[\frac{\partial}{\partial x}(huv)+\frac{\partial}{\partial y}(hv^2)\right)d\mathcal{S}+\int\int v\frac{\partial h}{\partial t}\,d\mathcal{S}+\int\int_{\mathcal{S}}(f_0+\beta y)(u+C)h\,d\mathcal{S}+\frac{g'}{2}\int\int_{\mathcal{S}}\frac{\partial}{\partial y}(h^2)\,d\mathcal{S}=0. \quad (5)$$

We now see that the second integral can be neglected (as *very* small) because the only asymmetrical part of v that can contribute to the integral is small and $\partial h/\partial t$ is also small. Note that $\mathcal{S}$ is a weak function of time due to the slowly shrinking lens and the slow translation of the coordinate system. This time-dependent variation can be neglected on the same grounds as our neglect of the other time-dependent terms. We now introduce a streamfunction defined such that $\partial\psi/\partial y = -uh$, and $\partial\psi/\partial x = vh$. Note that, with this definition, ψ is not exactly a constant along streamlines because $\partial h/\partial t$ is not exactly zero. An application of Green's theorem to (5) gives

$$\oint(huv-hv^2-g'h/2+f\psi)\,dl + C\int\int_{\mathcal{S}}fh\,d\mathcal{S}+\beta\int\int\psi\,d\mathcal{S}=0, \quad (6)$$

where dl is a line element along the path l (defined in Fig. 6). Of course, (6) is a general statement of the momentum balance. It is also valid in the $h\to 0$ limit. At this point it is important to recall that the leak's thickness is $O[\varepsilon^{1/2}H_i]$. It is easy to show (using geostrophy) that the widths of the leaks must be $O(\varepsilon^{1/2}R_i)$ because an application of the Bernoulli along $h=0$ shows that the velocities in the jet must be $O([g'H_i]^{1/2})$. This implies that the integrals of $g'h^2/2$ and $f\psi$ across the jet are very small [i.e., of relative $O(\varepsilon^{3/2})$] and can be neglected. Finally, at least one of the three variables h, u, and v vanishes on every point along l so that (6) can be written as

$$-\int_H^I hv^2\,dx+\int_D^E hv^2\,dx+C\int\int_{\mathcal{S}}(f_0+\beta y)h\,d\mathcal{S}+\beta\int\int_{\mathcal{S}}\psi\,d\mathcal{S}=0. \quad (7)$$

Equation (7) is almost our final integrated momentum balance and warrants some discussion. The first two terms represent the meridional forces due to the fluid leakage along the two walls, and are analogous to the force exerted on a rocket due to the ejection of mass. We will denote this the ''rocket force.'' The third term is the northward-integrated Coriolis force due to the westward migration of the lens, and the final term is the southward β force (resulting from a greater Coriolis force acting on fluid parcels during the northern portion of their orbit than during the southern portion). Due to the symmetry of the jets, the first two terms cancel each other out and (7) becomes

$$C\int\int_{\mathcal{S}}(f_0+\beta y)h\,d\mathcal{S}+\beta\int\int_{\mathcal{S}}\psi\,d\mathcal{S}=0. \quad (8)$$

This balance between the southward β force and the northward Coriolis force is identical to that considered by Nof (1981), except that here h and ψ are weakly time dependent. The balance holds regardless of the fluid's potential vorticity, but requires that the two rocket forces cancel each other.

b. Solution

Equation (8) can be evaluated by introducing the expansions $\psi=\overline{\psi}+\psi'$ and $h=\overline{h}+h'$, where the bars denote the solutions associated with a free, radially symmetric eddy on an f plane, and the primes denote perturbations introduced by β and the encounter of the eddy with the gap. Substituting the expansions into (7), and neglecting terms quadratic in perturbation, we obtain

$$C(t)\int\int_{\mathcal{S}}f_0\overline{h}(t)\,d\mathcal{S}+\beta\int\int_{\mathcal{S}}\overline{\psi}(t)\,d\mathcal{S}=0, \quad (9)$$

which is identical to the balance on a β plane for a lens drifting freely to the west (e.g., Nof 1981; Killworth 1983; Cushman-Roisin et al. 1990) except that, as mentioned, C, $\overline{h}$, and $\overline{\psi}$ are all now functions of time.

Substitution of the zero PV form of (1) into (9) yields

$$C(t)=-\frac{1}{12}\beta R(t)^2, \quad (10)$$

which is a time-dependent form of the Nof (1981) result. Note that $C(t)$ is three times the magnitude of the westward drift rate obtained by Nof (1999) for a lens encountering a solid wall (i.e., no gap).

Because the wall and β introduce only weak perturbations to the circular shape and the radius of the lens, its distance from the center of the gap (D) and the gap width (W) are related through the geometric relationship,

$$R(t)^2=D(t)^2+W^2/4, \quad (11)$$

illustrated in Fig. 6. Because the westward drift rate of the lens is given by $C=dD/dt$, (10) becomes

$$\frac{dD}{dt} = -\frac{\beta}{12}\left[D^2 + \frac{W^2}{4}\right], \tag{12}$$

which can be integrated and solved for $D(t)$,

$$D(t) = \frac{W}{2}\tan\left[\frac{1}{24}\tan^{-1}\left(\frac{2D_i}{W}\right) - W\beta t\right], \quad 0 \le t \le t_f, \tag{13}$$

where t_f is the soon to be computed encounter time. In deriving (13) we have used the boundary condition that, at the time of initial contact ($t = 0$), the distance of the lens center from the gap is $D_i = [W^2/4 - R_i^2]^{1/2}$.

Note that (13) applies only when the lens is in contact with the wall. For $t < 0$ (i.e., the lens is still in the eastern basin and has not yet reached the walls), the position of the lens is given by $D(t) = D_i + \int_t^{t=0} C_i\, dt$. For $t > t_f$ (i.e., the lens has lost contact with the walls and is in the western basin), the position of the lens is given by $D(t) = \int_{t=t_f}^{t} C_f\, dt$, where C_f is the final westward drift rate of the lens after it lost contact with the walls. The open ocean solution for D and its first derivative (dD/dt) are continuous at $t = 0$ and $t = t_f$, implying that the open ocean westward drift rates and the drift rate match at $t = 0$ and $t = t_f$.

Setting $D = 0$ in (13) and solving for $t = t_f$, we obtain the encounter time

$$t_f = \frac{24}{\beta D_i}\tan^{-1}\left(\frac{2D_i}{W}\right). \tag{14}$$

At the termination of the encounter ($t = t_f$), the lens center is collinear with the axis of the wall and the lens diameter is equal to the gap width. As expected, in the limit of a gap much smaller than the initial eddy radius (i.e., $W/R_i \to 0$), t_f becomes infinite, and, in the limit of a gap width equal to the initial eddy diameter [$W/(2R_i) \to 1$], t_f goes to zero.

We can determine $C(t)$ for the encounter from (10), (11), and (13),

$$C(t) = -\frac{\beta W^2}{48}\sec^2\left[\frac{W\beta t}{24} - \tan^{-1}\left(\frac{2D_i}{W}\right)\right], \quad 0 \le t \le t_f. \tag{15}$$

For $t \le 0$, the open ocean westward drift rate is $C = -(1/12)\beta R_i^2$, and, for $t \ge t_f$, the reduced open ocean westward drift rate is $C_f = -(1/48)\beta W^2$. Although the drift rates are continuous at $t = 0$ and $t = t_f$, the *time derivative* of C is discontinuous at $t = 0$ (i.e., when the eddy first makes contact with the wall). This occurs because $dC/dt = 2R\,(dR/dt)$ and dR/dt is discontinuous at the time of contact (because it is zero for $t < 0$, and nonzero for $t_f > t > 0$). In reality, of course, dC/dt is continuous at the time of initial impact, but the transition occurs over the fast timescale that has been eliminated from our slowly varying solution. (Note that dC/dt *is* continuous at $t = t_f$ because $dR/dt = 0$ at that time.) We shall see later that the numerics clearly reflect this behavior. The time-dependent volume of the lens is

$$V(t) = \frac{\pi f_0^2}{16g'}R(t)^4, \tag{16}$$

where $R(t)$ is obtained from (11) and (13). The final volume, given by

$$\frac{V_f}{V_i} = \left(\frac{W}{R_i}\right)^4, \tag{17}$$

remains constant after the lens leaves the gap. To give an appreciation for this quartic relationship, it is noted that a gap width that is half the diameter of the lens allows only 1/16 (<10%) of the fluid to penetrate into the interior of the western basin.

Finally, the mass flux out of the eddy, q, carried by the two jets is given by the time derivative of (16). The volume flux is discontinuous at $t = 0$ as a result of our slowly varying approximation. Thus, the flux is zero before the lens makes contact with the wall, but jumps to a finite value at $t = 0$.

Note that we do not recover the Nof (1999) eddy-wall solution as $W \to 0$ because our solution requires that the wall jets be *symmetrical*, whereas Nof required them to be *asymmetrical*. Further discussion of the solutions given by (10)–(17) is postponed until section 3 where a detailed comparison to the numerical experiments is made.

c. Collisions forced by advection

Because there is a basic flow through the passages of the LA (Table 1), advection is a likely component of a NBCR migration through the gaps of the LA. Up to now we have employed a traditional 1½-layer regime, where our active upper layer is resting on a quiescent lower layer. In order to address this advection in a simple way, we shall now consider a slight modification, whereby the lower layer is in motion but does not evolve in time. It is easy to show that the resulting pressure gradients in the lower layer act as a forcing term on the active layer.

We will now discuss the physics governing this advective flow through a gap. As mentioned, we consider the *steady* f-plane flow of a deep uniform layer of inviscid fluid; far upstream of the gap, the streamlines are parallel to the axis of the gap. Since the layer is inviscid, its potential vorticity will be $q = f/H_o$, where H_o is the very large upstream layer depth. In the vicinity of the gap, the layer's potential vorticity will be $(f + \zeta)/(\delta h + H_o)$, where δh is the perturbation to the layer thickness in the vicinity of the gap. The fluid's potential vorticity cannot change, and therefore as long as $H \gg \delta h$, ζ will be negligible everywhere. We shall focus on the limiting case where the fluid flow is governed by $\nabla^2\psi = 0$ (i.e., the flow results from a potential). The

analytical solution for such a flow through a gap is well known (e.g., Milne-Thompson 1968).

We recognize that *rotational* flow through a gap is a complicated problem, and is the subject of previous and current research (e.g., Nof 1995a,b; Sheremet 2001). In our case, however, we simply assert that the flow is steady, inviscid, and that the layer is infinitely deep so that potential flow is the correct model. Note that a similar use of potential flow to advect an eddy toward an obstacle was recently employed in the study of Stern (2000).

The streamlines of the lower layer flow converge as they pass through the gap, and the resulting strain distorts the lens. For the lens structure to vary only on the slow timescale, the lens must deform slowly when compared to the f-plane adjustment timescale. Although the convergence of the advecting flow through the gap makes the problem somewhat different from a β-induced collision, we define an analogous small parameter, $\mu = U/(f\mathrm{Ro}R_i) \ll 1$ (where U is the speed of the advecting flow at the center of the gap).

There are two different scenarios for the evolution of the lens as it is squeezed through a gap by advection. The first case is that of a very weak lens and strong advection [i.e., $\mu \sim O(1)$]. In this regime the dynamics governing the lens are unimportant in the sense that the fluid in the lens is a *slave* to the surrounding flow, and hence does not come into contact with the walls. Therefore, no jets can be established, and accordingly, the final volume of a slave lens is equal to its initial volume (i.e., $V_f/V_i = 1$). The second case is that of an intense lens ($\mathrm{Ro} = 1$) forced through a gap by weak advection ($\mu \ll 1$). In this case, the lens is *stiff* in the sense that it resists the strain induced by the advection, and, therefore, it must drain slowly via wall jets while the underlying fluid slips into the adjoining basin. Because the stiff lens does not distort, it advances *slowly* into the western basin as it shrinks. Its diameter is ultimately reduced to the gap width, and (provided that the lens conserves PV), the final volume of a stiff lens is again governed by the geometrical relationship (17). This latter case is very similar to the β-induced encounter.

3. Single gap numerical experiments

In this section we compare our theory with numerical simulations that explicitly include (albeit approximately) the detailed processes circumvented in the analytical solution. For our comparison with the theory (10)–(17), we varied W and fixed R_i, β, f_0, and g'. We also used the numerical model to investigate the detailed roles of ε, μ, and Ro, which are not addressed by our theory. For simplicity, we considered the roles of β and advection independently. A summary of the important model parameters can be found in Table 2.

Numerical experiments were conducted using the model described in section 1d. Even the narrowest gap was resolved by seven grid points. For runs employing β, we used an elevated value of 8.0×10^{-13} cm^{-1} s^{-1} (so that our runs were computationally efficient). The computational domain was divided into eastern and western basins. When advection was the lens propulsion mechanism, we determined the flow using a solution for potential flow through a gap. As mentioned, there is no interfacial friction, and the only coupling between the steady, advecting layer and the lens is via pressure forces. We defined the volume of the lens as the volume of fluid enclosed by the $h/H_i = 0.1$ contour.

a. β-induced collisions of intense lenses

Typical snapshots of the upper layer thickness of a lens as it was forced through a gap from a typical numerical experiment (expt 6) are shown on the left-hand side of Fig. 7. As expected, the lens remained quasi-circular, drained via narrow, symmetrical wall jets, and remained centered in the gap.

In Fig. 8 we present a comparison between the theoretical solution for $W/(2R_1) = 0.5$ and the numerics at two different resolutions, 8 km (expt 4) and 2 km (expt 7). The comparison is generally quite good, and clearly improves as the grid spacing is reduced. For our comparison with the theory, we defined the time of initial contact to be $t = 0$. For these two experiments, the analytically predicted total encounter time, t_f, was 27.5 days. The westward drift rate through the gap (15) (Fig. 8, panel 1) compares very favorably with the theory at both resolutions. The numerically computed drift rate was 10%–20% lower than the analytical drift rate for the low-resolution case, and 5%–10% lower for the high-resolution case. For reference, experiments conducted without lateral boundaries (expts 30–33) showed that even in the open ocean, the numerically determined westward drift rate is 10%–20% less than the theoretical value of $-(1/12)\beta R_i^2$. Thus, the presence of the gap added no additional errors. Notice that the rapid change in the numerically determined value of C at $t = 0$, where our analytical solution has a discontinuity in dC/dt.

The position of the lens relative to the gap (13) also compared well with the numerics (Fig. 8, panel 2). As expected, D and its time derivative were continuous at $t = 0$ and $t = t_f$. The discrepancy between the analytically and numerically predicted lens location was due to the discrepancy in C (seen in panel 1) that accumulated over the time of the encounter. Again, the agreement improved at the higher model resolution. We attribute this close agreement between the analytical solutions and numerical experiments to the fact that our analytical solution depends on *integrated* quantities that are relatively insensitive to the perturbations to the f-plane structure and also to the fact that the outcome is not critically sensitive to the inevitable numerical dissipation.

The lens radius and volume shrank a bit more slowly than expected (Fig. 8, panels 3 and 4), but the *final* values compared very well. Because the lens traveled

TABLE 2. Parameters for the single gap numerical experiments. The last four experiments (30–33) are reference experiments that were conducted without walls. For all experiments, $f_0 = 5 \times 10^{-5}$ s^{-1}, $g' = 0.9801$ cm s^{-2}, and the initial lens radius was 140 km. For the 8, 4, and 2 km experiments, the time step was 432, 216, and 108 s, respectively.

Expt	Propulsion mechanism	Δx, Δy (km)	β (cm^{-1} s^{-1})	$W/(2R_i)$	Ro	H_i (m)	ϵ	μ	Frictional coefficient (cm^2 s^{-1})
1	β	8	8×10^{-13}	0.8	1	600	0.02	0.00	6.0×10^6
2	β	4	8×10^{-13}	0.6	1	600	0.02	0.00	3.0×10^6
3	β	8	8×10^{-13}	0.6	1	600	0.02	0.00	6.0×10^6
4	β	8	8×10^{-13}	0.5	1	600	0.02	0.00	6.0×10^6
5	β	8	8×10^{-13}	0.4	1	600	0.02	0.00	6.0×10^6
6	β	4	8×10^{-13}	0.4	1	600	0.02	0.00	6.0×10^6
7	β	2	8×10^{-13}	0.5	1	600	0.02	0.00	1.5×10^6
8	β	8	8×10^{-13}	0.7	1/4	600	0.01	0.00	6.0×10^6
9	β	8	8×10^{-13}	0.5	1/4	600	0.01	0.00	6.0×10^6
10	Advection	4	0	0.2	1/4	270	0.00	0.12	3.0×10^6
11	Advection	4	0	0.2	1	600	0.00	0.06	3.0×10^6
12	Advection	4	0	0.2	1/4	270	0.00	0.47	3.0×10^6
13	Advection	4	0	0.1	1	600	0.00	0.34	3.0×10^6
14	Advection	4	0	0.3	1/4	270	0.00	0.13	3.0×10^6
15	Advection	4	0	0.3	1	600	0.00	0.07	3.0×10^6
16	Advection	4	0	0.3	1/4	270	0.00	0.59	3.0×10^6
17	Advection	4	0	0.3	1	600	0.00	0.29	3.0×10^6
18	Advection	4	0	0.5	1/4	270	0.00	0.11	3.0×10^6
19	Advection	4	0	0.5	1	600	0.00	0.06	3.0×10^6
20	Advection	4	0	0.5	1/4	270	0.00	0.55	3.0×10^6
21	Advection	4	0	0.5	1	600	0.00	0.28	3.0×10^6
22	Advection	4	0	0.7	1/4	270	0.00	0.10	3.0×10^6
23	Advection	4	0	0.7	1	600	0.00	0.05	3.0×10^6
24	Advection	4	0	0.7	1/4	270	0.00	0.53	3.0×10^6
25	Advection	4	0	0.7	1	600	0.00	0.26	3.0×10^6
26	Advection	4	0	0.9	1/4	270	0.00	0.09	3.0×10^6
27	Advection	4	0	0.9	1	600	0.00	0.04	3.0×10^6
28	Advection	4	0	0.3	1/4	270	0.00	0.03	3.0×10^6
29	Advection	4	0	0.1	1/4	270	0.00	0.45	3.0×10^6
30	β	4	8×10^{-13}	N/A	1	600	N/A	N/A	3.0×10^6
31	β	4	8×10^{-13}	N/A	1	600	N/A	N/A	6.0×10^6
32	β	2	8×10^{-13}	N/A	1	600	N/A	N/A	1.5×10^6
33	β	8	8×10^{-13}	N/A	1	600	N/A	N/A	6.0×10^6

somewhat slower than expected in the numerical experiments (panels 1 and 2), the value of R and V lagged in time behind the analytical value, but finally caught up as the lens lost contact with the gap. Thus, the geometric constraints (11) and (17) are valid during the entire encounter.

As expected, the Coriolis and β forces (9) nearly balanced (Fig. 8, panel 5). For clarity, we only show the force balance for experiment 4; the results are very similar for all of the experiments. Although space precludes presentation of a detailed analysis of the terms contributing to Eq. (6) [the precursor to Eq. (9)], we found that the six terms in Eq. (6) were typically of relative order ε^3, ε^2, ε^2, $\varepsilon^{3/2}$, ε^1, ε^1, respectively. This is consistent with our scaling. The numerically and analytically computed mass flux out of the lens, q, also agreed well during the encounter. Notice the discontinuity in the analytical solution at $t = 0$, when the jets are established ''instantly'' (i.e., on the fast timescale). In the numerical solution, the jets are established over several days. After day 4, the analytical and numerical solutions agree very well.

The agreement of the final volume of the lens for all β-forced single gap numerical experiments and the analytically predicted final volume (17) (Fig. 9a) is quite good. The total encounter time t_f is shown in Fig. 9b. The agreement is excellent for broad gaps [$W/(2R_1) \rightarrow 1$], but for narrower gaps the numerical lenses take an increasingly longer time relative to the analytical solution. This is consistent with the systematically smaller drift rate in the numerical experiments; the discrepancy becomes more pronounced for narrower gaps because the difference accumulates over the longer encounter times.

b. β-*induced collisions of weak lenses*

We conducted two experiments with weak (Ro = 1/4) lenses (expts 8 and 9). These lenses remained circular and drained slowly in a manner similar to that seen in the left-hand side of Fig. 7. We did not solve (9) for weak lenses, but we expect that their final volume will also be determined by the geometrical relationship (17) because the volume of any lens described by (1) is proportional to the fourth power of the eddy's radius. This comparison is quite good (Fig. 9a).

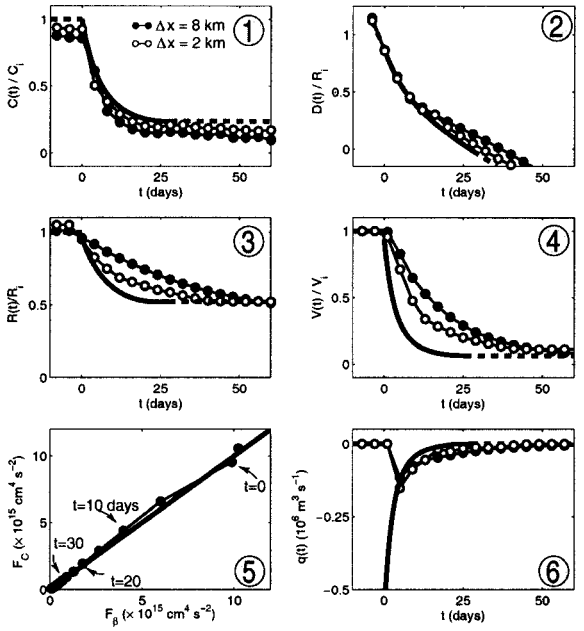

FIG. 8. A comparison of the analytical and numerical solutions for an eddy forced by β through a single gap of width $W/(2R_i) = 0.5$. The thick solid lines show the analytical solution for the time that the lens is in contact with the gap and the dashed lines show the open ocean analytical solutions. The solid circles indicate results from experiment 4, and the open circles indicate results from experiment 7. Both numerical experiments are configured with identical geometries, but experiment 4 is run at 8-km grid spacing, whereas experiment 7 is run at 2-km grid spacing. Note that the agreement improves for the higher resolution experiment. Panel 1 shows the westward drift rate (15) scaled by the open ocean drift rate. Panel 2 shows the distance of the eddy's center from the center of the gap (13) scaled by the initial lens radius, R_i. Panel 3 shows the eddy's radius and panel 4 shows the volume reduction. Panel 5 shows the numerically calculated integrated β force, $\mathbf{F}_\beta$ vs the numerically calculated integrated Coriolis force, $\mathbf{F}_c$ at various times. Finally, panel 6 shows the volume flux, q, carried by the jets as a function of time.

c. Advection of intense lenses

Intense lenses are stiff and hence able to resist the strain of the advective flow through the gap (center column of Fig. 7). We compared the final volume of intense (Ro = 1) lenses forced by an advecting flow through a gap of width W with the volume predicted by (17) (Fig. 10a). The agreement (or lack thereof) provides one measure of the ability of the lens to resist the strain induced by the advecting flow.

The coupling of weak lenses to the advecting fluid is also revealed by the difference between the translation rate of the thickest point in the lens and the corresponding velocity in the adjoining lower layer (Fig. 11). We found that intense lenses ''stalled'' in front of the gap while the underlying fluid slipped into the western basin (e.g., expt 13 in Fig. 11). In this regime, zero PV lenses did not significantly distort; they drained slowly via wall jets until their diameter was equal to the gap width, at which point they were swept into the downstream basin (center column of Fig. 7). Thus, the agreement with the geometrical relationship (17) was quite good for both weak and strong advection, but was best when the advection was weakest ($\mu < 0.3$). When the advection was stronger ($\mu > 0.3$) there was some minor distortion of the lens, but the lens drained much more slowly than would be expected were it simply a slave to the lower layer.

d. Advection of weak lenses

In contrast to the β-forced collisions discussed in section 3b, *weak* lenses were slaves to the advection, and hence were almost entirely squeezed through the gaps, experiencing considerably less drainage than predicted by (17) (see the right panel of Fig. 7, and Fig. 10b). In experiment 16, for example, the lens was violently distorted by strain from the advection through the gap and was carried through with little contact with the walls (right-hand column of Fig. 7). Even though the gap width was no more than $0.15R_i$, more than 80% of the fluid contained in the initial lens remained in the lens. For the smallest gaps in this regime (e.g., expt 29), with a dimensional gap width of 28 km, $W/2R_i = 0.1$, and 40% of the lens squeezed through the gap. Were the drainage to be governed by (17), only 0.2% of the initial volume would have remained in the lens. The distortion induced by the advection did not entirely prevent the lens fluid from coming into contact with the walls, and hence some drainage occurred. Thus, the final volume falls somewhere between $V_f/V_i = 1$ and $V_f/V_i = (W/R_i)^4$. For a weak lens, only when the advection was *extremely* weak (e.g., expt 28, where $\mu \approx 10^{-2}$) did we recover the final volume reduction described by (17).

The slaving of the lens to the advective flow was clearly evident in experiment 24 (Fig. 11). Note that, at times, the translation of the thickest point in the lens *exceeded* that of the advecting layer at the center of the gap, probably because the speed near the tips of the walls was quite high. (Because the advecting layer is governed by potential flow and the walls are lamina, the theoretical speed at the tips of the walls is infinite. However, the C grid is arranged so that the walls do not lie on velocity points. Thus, in the discrete numerical model, the velocity at the wall tips is finite.)

e. Summary of single gap theory and numerical experiments

1) For β-induced collisions, both weak and intense lenses drain via wall jets, and the final volume is given by the geometric relationship (17).
2) Intense lenses are stiff in the sense that they are able to resist the strain induced by advection through the gap. Thus, the final volume of the lens is described by (17).
3) On the other hand, weak lenses are squeezed by the convergent advective flow through the gap, and the

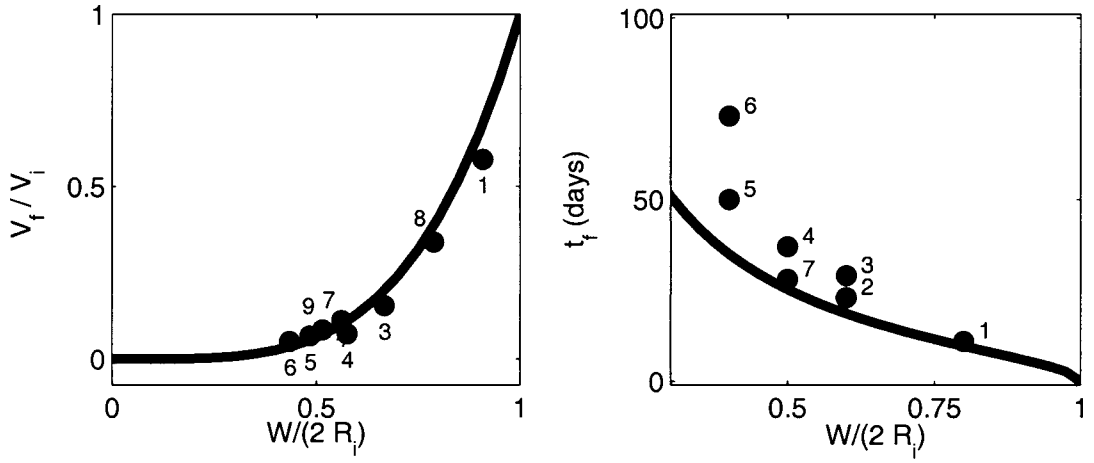

FIG. 9. A comparison of the numerical and analytical determined final volume (a: left) and total encounter time (b: right) for our β-induced eddy/single gap numerical experiments. (a) A comparison of the final volume of the eddy (which enters the western basin due to β) and the volume predicted by the geometrical constraint $V_f/V_i = (W/R_i)^4$. The agreement is excellent. (b) A comparison of the analytically predicted and numerically computed total encounter time, t_f (i.e., the elapsed time from the moment that the eddy first makes contact with the walls to the time that it loses contact with the walls). The agreement is good for broader gaps. The discrepancy is due to the slower drift rates of the lens in the numerical experiments. This difference between the numerical and analytical drift rates accumulates over time so that the discrepancy is greatest for narrow gaps where the encounters are longest. Note that the agreement improves for higher resolution numerical experiments (e.g., expt 7 vs 4). The experiment numbers are labeled next to their respective circles.

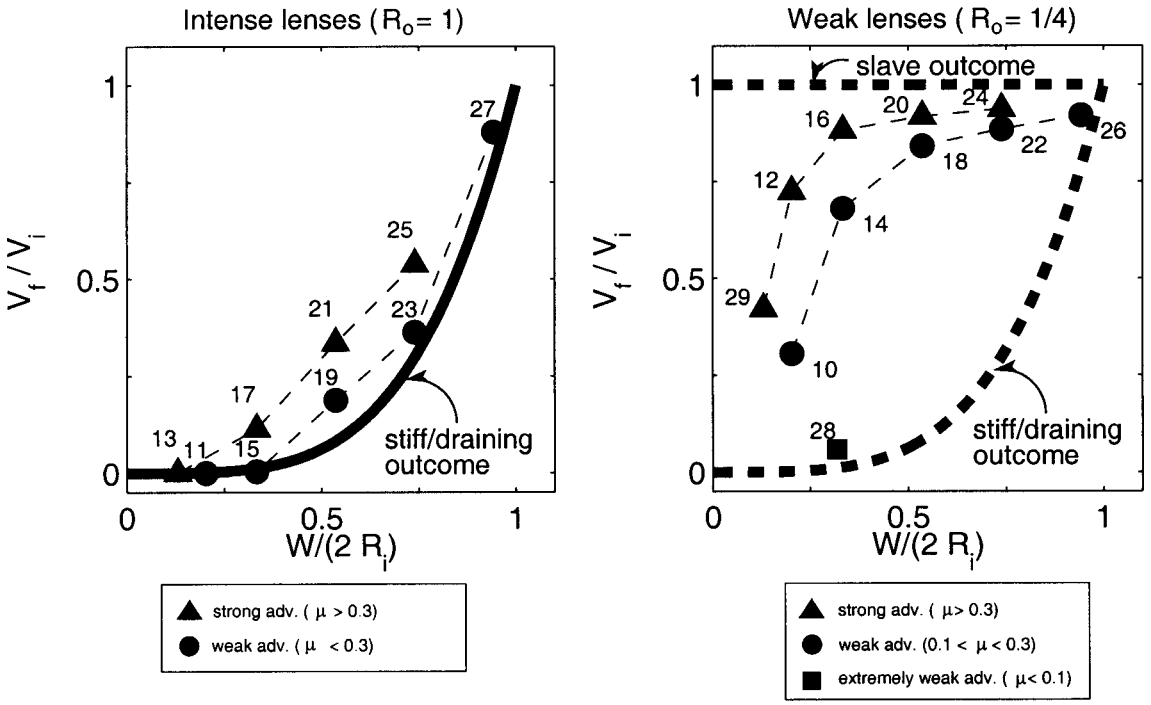

FIG. 10. A comparison of the final (numerical) volume of the eddy that enters the western basin due to advection, with the final volume predicted by the draining relationship $V_f/V_i = (W/R_i)^4$, and the final volume predicted by the slave relationship $V_f/V_i = 1$. The numerals indicate the experiment number. Intense lenses are stiff and hence are drained by wall jets (a: left). Notice that both strongly forced collisions ($\mu > 0.3$) and weakly forced collisions ($\mu < 0.3$) fall fairly close to the curve defining the draining relationship, and that the agreement is better for weaker forcing. Weak lenses are slaves to the advection, and hence, a great deal more fluid is forced through the gap (b: right). Note that, in the weak lenses case, the draining relationship is approached only for small gaps and for extremely weak advection (e.g., expt 28). For intermediate values of W, the outcome is a combination of the draining and slave relationships.

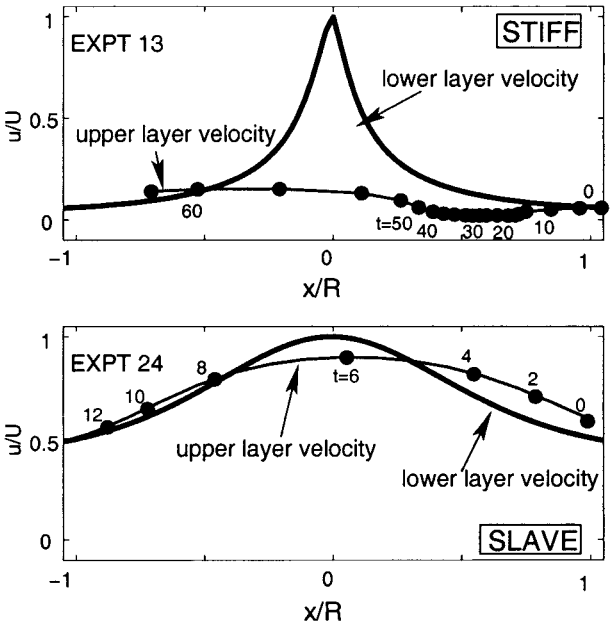

FIG. 11. A comparison between the translation rate of the thickest point in the lens (circles) and the corresponding velocity (solid line) of the underlying fluid. The numerals indicate the time (in days). Velocities are scaled by U, the velocity of the lower layer at the center of the gap. (a) experiment 13, the lens is intense, the gap is narrow [$W/(2R_i) = 0.1$], and, as a result, the lens stalls in front of the gap. This can be seen by the difference between lower layer velocity and the lens migration rate, as well as by the crowding of circles reflecting the slow translation of the lens center from day 10 to 50. On the other hand, in (b) experiment 24, the lens is weak and the gap is broad [$W/(2R_i) = 0.7$] so that the lens is a slave to the advecting flow. Curiously, from day 0 to 4 and from day 8 to 12, the advection speed of the lens center actually *exceeds* that of the underlying fluid.

ratio of the final volume to the initial volume of the lens falls somewhere between $(W/R_i)^4$ and unity. Stronger advection makes the outcome fall closer to unity (a slavelike lens) and weaker advection makes the outcome fall closer to $(W/R_i)^4$ (a stiff, draining lens).

4. Multiple gap numerical experiments

For the multiple-gap experiments we used the same reduced-gravity model of a zonal channel as in the single-gap experiments. The meridional extent of the channel was 1000 km, which is the approximate meridional width of the entrance to the Caribbean Sea, and all boundaries were free slip. We again considered β and advection as propulsion mechanisms. Our eddies were 300 km in diameter. Because the effect of varying the gap width was already explored in detail in the previous sections, we restricted ourselves here to a single gap width [$W/(2R_i) = 0.2$], which was chosen to reflect the NBCR/LA collisions. We explored three different island sizes ($L/R_i = 0.3$, 0.5, and 1.5), also chosen to represent the range of island sizes present in the LA. The ratio $L/R_i = 0.3$ is somewhat smaller than the typical value for islands of the LA, $L/R_i = 0.5$ is typical of the many islands of the LA (e.g., St. Vincent or Martinique, see Figs. 1 and 2), and $L/R_i = 1.5$ is larger than most of the LA (except the Grenadines, see Figs. 1 and 2).

We explored the sensitivity of the outcome to the initial position of the lens by varying the offset parameter, y_0 (see Fig. 4). The various combinations of collision mechanism (β or advection), wall length ($L/R_i = 0.3$, 0.5, or 1.5), offset ($y_0/R_i = -0.3$, 0, or 0.3), and lens intensity (Ro = 1/4 or Ro = 1) resulted in 27 different combinations of parameters (expts 34–60, Table 3). [The reason that there were only 27 experiments conducted, as opposed to 36, is that weak lenses were only forced by advection.] Again our lens propulsion mechanisms (β or advection) were explored in isolation, not in concert. The eddy was initialized with (1) using the appropriate value of Ro. Experiment 61 explored the role of nonvanishing upper layer thickness [i.e., we added a constant value to the layer thickness in (1)]. Details of the model configuration for all 28 experiments are given in Table 3.

a. General description of the eddy/multiple gaps collision

As a result of the additional gaps, the lens fluid was not ultimately trapped near the walls as jets but rather penetrated into the interior of the western basin. Depending on the parameters used, the lens either entered the western basin as a coherent feature or broken up into a number of smaller lenses. We will organize our discussion according to the island size because it is the variations of this parameter that produced the main differences in the outcome. As in the single gap experiments, the volume of a lens is defined by the fluid enclosed by the $h/H_i = 0.1$ contour.

The processes involved in the squeezing of a lens through multiple gaps are illustrated schematically in Fig. 12. Recall that the single-gap numerical experiments and theory demonstrated that if the eddy is *intense* or is forced by β, it remains quasi-circular, and cannot pass through a gap until the wall jets have removed enough volume for it to lose contact with the gap (Fig. 12 left). The response of the eddy to the local gap is very much like this single gap case. As in the single gap case, a weak lens is a slave to advective flow through an individual gap (Fig. 12 right); an intense lenses is stiff and stalls at the boundary, decoupled from the advective flow through the gap (Fig. 12 center). The critical difference in the multiple gap case is the fate of the wall jets. Our gap width of $0.2R_i$ required that the wall jets split and partially retroflect when they reached a downstream gap (see Fig. 12). This retroflection must form an eddy in order to balance the momentum flux of the jets (Nof and Pichevin 1996). When the separation of the gaps (determined by the length of the wall L) is sufficient, these secondary eddies pinch off and drift into the western basin. This results in the breakup of

TABLE 3. Parameters for the multiple gap numerical experiments. Most of the column headings are self-explanatory. Specifically H_∞ is the upper layer depth outside the eddy, N gives the total number of offspring produced by the collision, and the V fraction gives the volume of each offspring (scaled by the total fluid accounted for in the final state). For all experiments, the time step was 432 s, $f_0 = 5 \times 10^{-5}$ s^{-1}, $g' = 0.9801$ cm s^{-2}, $R_i = 144$ km, the horizontal grid spacing was 4 km, and the Laplacian friction coefficient was 4×10^6 cm^2 s.$^{-1}$ The parameters for single gap numerical experiments 1–33 are given in Table 2.

Expt	Propulsion mechanism	L/R_i	y_0/R_i	Ro	H_i (m)	H_∞ (m)	β (cm^{-1} s^{-1})	ϵ	μ	N	V fraction
34	β	0.3	0.3	1	600	0	6×10^{-13}	0.02	0.00	2	0.95, 0.05
35	β	0.3	0.0	1	600	0	6×10^{-13}	0.02	0.00	2	0.95, 0.05
36	β	0.3	−0.3	1	600	0	6×10^{-13}	0.02	0.00	2	0.95, 0.05
37	Advection	0.3	0.3	1/4	270	0	0	0.00	0.20	1	1.00
38	Advection	0.3	0.0	1/4	270	0	0	0.00	0.20	1	1.00
39	Advection	0.3	−0.3	1/4	270	0	0	0.00	0.20	1	1.00
40	Advection	0.3	0.3	1	600	0	0	0.00	0.20	1	1.00
41	Advection	0.3	0.0	1	600	0	0	0.00	0.20	1	1.00
42	Advection	0.3	−0.3	1	600	0	0	0.00	0.20	1	1.00
43	β	0.5	0.3	1	600	0	6×10^{-13}	0.02	0.00	2	0.57, 0.43
44	β	0.5	0.0	1	600	0	6×10^{-13}	0.02	0.00	2	0.98, 0.02
45	β	0.5	−0.3	1	600	0	6×10^{-13}	0.02	0.00	2	0.85, 0.15
46	Advection	0.5	0.3	1/4	270	0	0	0.00	0.30	1	1.00
47	Advection	0.5	0.0	1/4	270	0	0	0.00	0.30	2	0.97, 0.03
48	Advection	0.5	−0.3	1/4	270	0	0	0.00	0.30	1	1.00
49	Advection	0.5	0.3	1	600	0	0	0.00	0.20	1	1.00
50	Advection	0.5	0.0	1	600	0	0	0.00	0.20	1	1.00
51	Advection	0.5	−0.3	1	600	0	0	0.00	0.20	2	0.97, 0.03
52	β	1.5	0.3	1	600	0	6×10^{-13}	0.02	0.00	2	0.71, 0.29
53	β	1.5	0.0	1	600	0	6×10^{-13}	0.02	0.00	4	0.59, 0.36, 0.04, 0.01
54	β	1.5	−0.3	1	600	0	6×10^{-13}	0.02	0.00	4	0.76, 0.15, 0.06, 0.03
55	Advection	1.5	0.3	1/4	270	0	0	0.00	0.60	2	0.64, 0.36
56	Advection	1.5	0.0	1/4	270	0	0	0.00	0.60	2	0.65, 0.35
57	Advection	1.5	−0.3	1/4	270	0	0	0.00	0.60	3	0.88, 0.07, 0.05
58	Advection	1.5	0.3	1	600	0	0	0.00	0.20	3	0.91, 0.06, 0.03
59	Advection	1.5	0.0	1	600	0	0	0.00	0.20	3	0.75, 0.18, 0.07
60	Advection	1.5	−0.3	1	600	0	0	0.00	0.20	3	0.50, 0.30, 0.20
61	β	0.5	0.0	1	600	150	6×10^{-13}	0.02	0.00	3	0.65, 0.20, 0.15

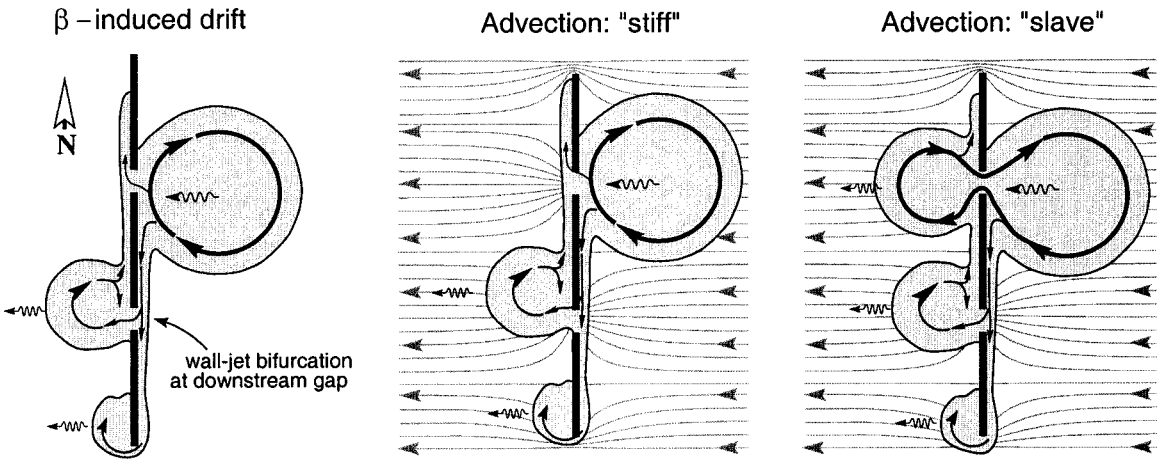

FIG. 12. The impingement of an eddy on a boundary containing multiple gaps (adapted from our numerical experiments). The wiggly arrows denote propagation. The collision due to β (left). As in the single gap case, the lens–wall encounter initiates drainage via wall jets. The jet retroflections at the downstream gaps are potential offspring lens formation sites. When the distance separating the gaps is smaller than shown here, the offspring ''kiss'' and then remerge. On the other hand, when the distance between the gaps is large enough (as is illustrated here), the offspring are separated spatially and, consequently, do not merge in the western basin (cf. with the left-hand side of Fig. 7). The collision due to advection (center) of an intense lens (with the streamline of the advective flow indicated in gray). The lens is stiff and drains slowly via wall jets (cf. with the center column of Fig. 7). The collision due to advection (right) of a weak lens. The eddy strikes the central gap and the resulting flow patterns are locally similar to the single gap slave case with wall jets partially draining fluid to the north and south and the lens partially squeezing through the gap (cf. with the right-hand column of Fig. 7).

the initial lens into multiple offspring. On the other hand, when the spacing is not large, the offspring come into contact with each other as they grow and hence remerge. To summarize, in the closely spaced gap regime (i.e., short walls), the eddy ultimately enters the western basin as a single feature, whereas in the widely spaced gap scenario (i.e., long walls), the eddy ultimately breaks up. Although the ''slave'' and ''stiff'' categories also apply to the multiple gaps collisions when advection is the lens propulsion mechanism, we will concentrate on the ''splitting'' and ''nonsplitting'' issue here.

b. Small islands ($L/R_i = 0.3$)

When $L/R_i = 0.3$ (expts 34–42), the lens broke up and passed into the adjoining basin via several passages but ultimately reformed into a single coherent structure in the western basin (see Table 3 and Fig. 13). Experiments employing β as the collision mechanism resulted in a small amount of fluid (<5% of the total volume) being stripped from the eddy (similar to expt 35 pictured in Fig. 13). These small stripped patches of fluid remained near the islands. Given long enough integration times, β would eventually cause these patches to enter the western basin, migrating at a rate proportional to their amplitude. Understandably, with such small islands, variation of the offset, y_0, had little effect on the outcome.

Interestingly, as compared with intense lenses, weak lenses experienced relatively small loss of amplitude and were more compact in their final state (Fig. 13). For instance, experiment 35 (an intense lens) suffered an energy loss of 80% and an amplitude decrease of 50%, whereas experiment 38 (a weak lens) experienced an energy loss of only 30% and an amplitude decrease of only 20%. An intense lens experiences greater amplitude and energy loss than the weak eddies because friction acts preferentially upon the much larger velocities present in the intense lenses.

c. Medium islands ($L/R_i = 0.5$)

When the island length was increased to half the initial eddy radius, we began to see both hints of eddy breakage and a sensitivity of the final configuration to y_0 (expts 43–51). In the collisions employing β we found that, while there was a well-defined core of fluid that penetrated into the western basin, small blobs of fluid were stripped away from the original eddy. This was most pronounced in experiment 43, where the largest lens contained only 57% of the total fluid accounted for in the final state. When advection was the collision mechanism, this effect was very small and the outcome was more like that seen in Fig. 13 (expts 35 or 48). Again, relative to intense lenses, weak eddies seemed to maintain tighter structure and experienced less relative energy loss in the final state. These experiments suggest that an island length of $L/R_i = 0.5$ is on the threshold of inducing lens breakage. This effect is most pronounced for intense eddies propelled by β.

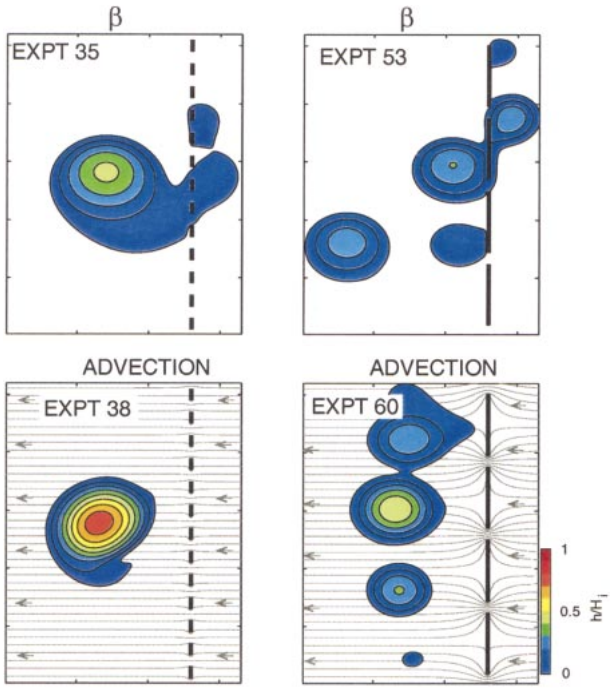

FIG. 13. Snapshots of final layer thicknesses illustrating the various regimes in our multiple-gap numerical experiments. The top two panels show collisions forced by β. Bottom two-panels show collisions forced by advection. In the latter case, contours of the advecting flow's streamfunction are indicated by the light gray lines. The left panels show that when the walls are short (e.g., $L/R_i = 0.3$, expt 35 and 38), the lens breaks up as it passes through the numerous passages, but ultimately reforms as a single coherent vortex in the lee of the wall. When the walls are long (e.g., $L/R_i = 1.5$, experiments 53 and 60), the lens is broken up into a number of smaller offspring. Also, note that the lenses are scaled by their respective initial thickness so that experiment 35 (which is initialized with an intense lens) is scaled by an initial dimensional layer thickness of 600 m, whereas experiment 38 (which is initialized with an weak lens) is scaled by an initial dimensional layer thickness of 270 m. This allows us to assess the relative loss of amplitude in the final state; it is clear that experiment 35 has lost a great deal more of its amplitude (50%) than experiment 38 did (20%).

d. Large islands ($L/R_i = 1.5$)

When the island length was further increased to $L/R_i = 1.5$ (expts 52–60), the lens broke into a number of offspring. Outcomes in this regime are similar to experiment 60 (Fig. 13). The total number of offspring were similar in all the experiments for this wall-length regime. The minor differences in the number of offspring and the mass partitioning between them are attributed to variations in y_0 (Table 3). With advection, the offspring lenses were aligned meridionally (Fig. 13, expt 60). For experiments employing β, the zonal distance between the offspring lenses in the lee of the archipelago increased over time (expt 53, Fig. 13) be-

cause the amplitudes of the individual offspring and, hence, their β-induced westward migration rates were not identical. Note that the final distribution of offspring almost filled the channel in the north–south direction (expt 60, Fig. 13).

e. Is the circulation around the islands constant in time?

Our multiple gaps numerical experiments show (Figs. 12 and 13) that the circulation does not remain constant around the individual islands. This is unusual as Pedlosky et al. (1997) [see also Pedlosky and Spall (1999) and Pedlosky (2000)] determined that the circulation should remain constant for continuous flows around islands. As we shall shortly see, our circulation is due to discontinuities near island tips absent from the runs of Pedlosky et al. (1997). Furthermore, it turns out that, since our problem varies slowly in time, even a very weak nonlinearity is sufficient to cause variations of $O(1)$ in our island circulation.

To see this, we first note that, in a reduced-gravity model with a surfacing interface such as ours, the velocities are always of $O[(g'H)^{1/2}]$ no matter how large (or small) the feature is, implying that some nonlinearity is always present and that, consequently, the model does not have a linear limit. In order to investigate the circulation in a simple regime, consider the lens/single island problem shown in Fig. 14. Using (2), (3) can be written as

$$\frac{\partial}{\partial t}(hv) + \frac{\partial}{\partial x}(huv) + \frac{\partial}{\partial y}(hv^2) + fuh + \frac{g'}{2}\frac{\partial}{\partial y}(h^2) = 0, \tag{18}$$

where, for simplicity, our coordinate system is now taken to be stationary. Equation (18) can be integrated along the western and eastern boundaries ($u = 0$) of the narrow island to give

$$\frac{\partial}{\partial t}\oint hv\,dy + \oint \frac{\partial}{\partial x}(huv)\,dy + \frac{g'}{2}[(h^2)|_C - (h^2)|_D] + \frac{g'}{2}[(h^2)|_A - (h^2)|_B] + [(hv^2)|_C - (hv^2)|_D] + [(hv^2)|_A - (hv^2)|_B] = 0. \tag{19}$$

When the nonlinear terms (hv^2, h^2) are neglected, (19) reduces to the familiar conservation of circulation condition

$$\frac{\partial}{\partial t}\oint hv\,dy = 0, \tag{20}$$

which was discussed by Pedlosky et al. (1997), Pedlosky and Spall (1999), and Pedlosky (2000).

We now present an analysis of the circulation source terms in (19) for an experiment where our zero PV eddy is forced by β into a single thin meridional island (Fig. 15). Note that all circulation terms have been scaled by v_w; h_w; L_w; T_w^{-1}, where $h_w = \varepsilon^{-1/2}H_i$ is a scale for the thickness of the jet along the wall, L_w is the length of the wall, $v_w = (g'H)^{1/2}$ is a scale for the velocities in the jet, and $T_w = L_w(g'H)^{-1/2}$ is the timescale over which the jet is established. We see that the dominant source for the change of circulation in time is the discontinuity in the term (hv^2), which is attributed to the flow separating from the wall tips. Moreover, since the process is slowly varying in time, even a small discontinuity in (hv^2) is sufficient to cause a gross violation of (19). Note that this conclusion also holds for Simmons and Nof (2000), where a similar setup of circulation occurred.

f. Finite upper layer depth

We also conducted a single experiment initialized with a finite resting upper-layer depth (i.e., $h \neq 0$ around the eddy). For this experiment, the island size was $L/R_i = 0.5$, β was the propulsion mechanism and the resting upper layer depth was equal to 1/4 of the zero PV lens amplitude. In this case the eddy broke up into three offspring. The presence of β and a finite upper-layer depth greatly enhanced the tendency for the eddy to break up, so that the outcome appeared to be very similar to the $L/R_i = 1.5$ outcome (i.e., similar to experiment 60 shown in Fig. 13).

g. Multiple gap summary

The main conclusions of our multiple gap numerical experiments are

1) Small islands (e.g., $L/R_i = 0.3$) allow a lens to penetrate into the western basin as a coherent structure.
2) Islands of intermediate size (e.g., $L/R_i = 0.5$) allow a lens to penetrate into the western basin as a coherent structure, but a tendency of the lens to break up was noted. This tendency is accentuated by the presence of β or a finite resting upper layer thickness.
3) Large islands (e.g., $L/R_i = 1.5$) always split an eddy into multiple offspring. It is appropriate to point out here that for a single wall aligned with the axis of translation of the eddy, Simmons and Nof (2000) showed that a wall length of $1.19R_i$ is sufficient for splitting.
4) As in the single-gap experiments, the eddy's intensity affects how much of the lens fluid can be forced

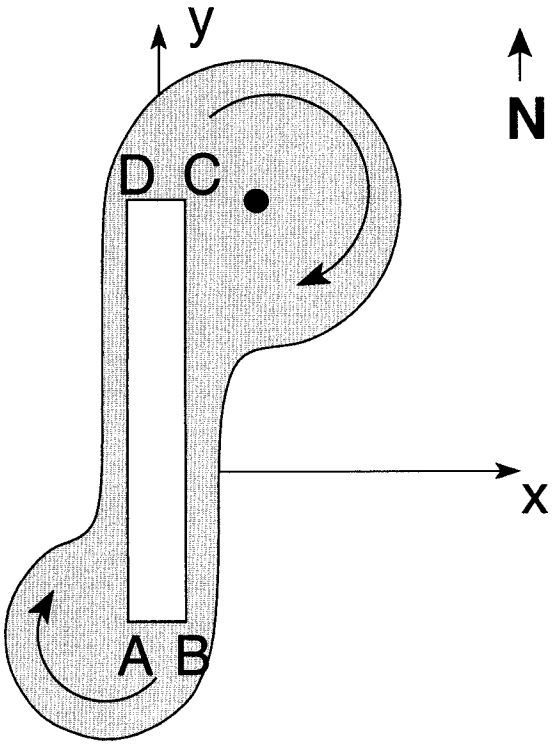

FIG. 14. A diagram of an eddy colliding with a narrow meridional island (adapted from our numerical experiments). Note that the flow has a tendency to separate from the tips **B** and **D** and that most of the flow surrounding the island has a boundary current structure.

through an individual gap; weak lenses are slaves to advection, and intense lenses are stiff.
5) Intense lenses experienced relatively greater amplitude loss than weak lenses.
6) The circulation around the islands is attributed to nonlinear flow separations at the tips of the islands.

5. Application to North Brazil Current rings

Based on a typical ring radius of 100–150 km at 8°N (Richardson et al. 1994), one can determine that β probably contributes approximately 2–4 cm s^{-1} to the 10–15 cm s^{-1} observed drift rate of NBCRs. The large observed drift speed is at least partly due to advection by the mean flow. Therefore, collisions due to advection are probably relevant to the study of NBCRs. Observations suggest the following parameters are typical for collisions with the LA:

- Lens Rossby number (Ro) of 0.2–0.4 (Richardson et al. 1994).
- Maximum swirl speed (v_θ) of 100 cm s^{-1} (Fratantoni et al. 1995).
- Mean surface velocity in the passages (U) of 20–40 cm s^{-1} (Wilson and Johns 1997).
- Lens radius (R) of 100 km (Richardson et al. 1994).
- Gap width (W) of 30 km $\approx 0.2R_i$ (Smith and Sandwell 1997).
- Island scale (L) of 50–200 km $\approx 0.3R_i - 1.5R_i$ (Smith and Sandwell 1997).
- Collision intensity (μ) of 0.2–0.4.

a. Single gap theory and experiments

The single gap experiments that are most applicable to the LA are experiments 10 (Ro = 1/4, μ = 0.12) and 12 (Ro = 1/4, μ = 0.47), where about half of the initial lens volume penetrates into the interior of the western basin through an individual gap (Fig. 10). Thus, it is unlikely that more than half of the fluid from an NBCR can be squeezed through an individual passage in the LA. It should be noted, however, that the region representing the NBCRs in Fig. 10 (e.g., in the vicinity of expts 10 or 12) falls on a very steep portion of the curves so that small differences in the collision strength, the NBCR size, or the intensity can have a large impact on the volume of fluid that can be squeezed through an individual gap.

b. Multiple gap experiments

The multiple gap experiments demonstrated that the islands that obstruct the entrance to the LA are near a size that can fragment NBCRs. NBCRs come in a broad range of sizes and intensities, and we have the rather counterintuitive result that a large, weak eddy is more likely to survive the passage into the LA as a coherent feature (e.g., expt 38, Fig. 13) than a small intense lens, which would likely be broken up (e.g., expt 60, Fig. 13). The dependence of the collision on the eddy strength arises because intense lenses are stiff and hence stall at the LA, resisting the mean flow. Any northward component of mean flow into the LA would thus cause an intense NBCR to slip to the north of the Antilles, whereas weak lenses would flow into the Caribbean Sea with the mean flow. Additionally, we found that intense lenses experience relatively greater dissipation. The dependence on eddy size arises, rather trivially, because we have considered the ratio of eddy radius to island length. Because the island of the Lesser Antilles are of a fixed length, it is the variations of initial eddy radius that dictate L/R_1, and, hence, whether or not the LA are large enough to break up an NBCR.

6. Limitations

As is the case with any new problem, a number of necessary simplifications had to be made. Specific deficiencies in our study were:

- *The adoption of a reduced-gravity model of a uniform relative vorticity eddy.* Although many ocean eddies have been observed to have cores of this type, real ocean eddies are not inviscid lenses. They are em-

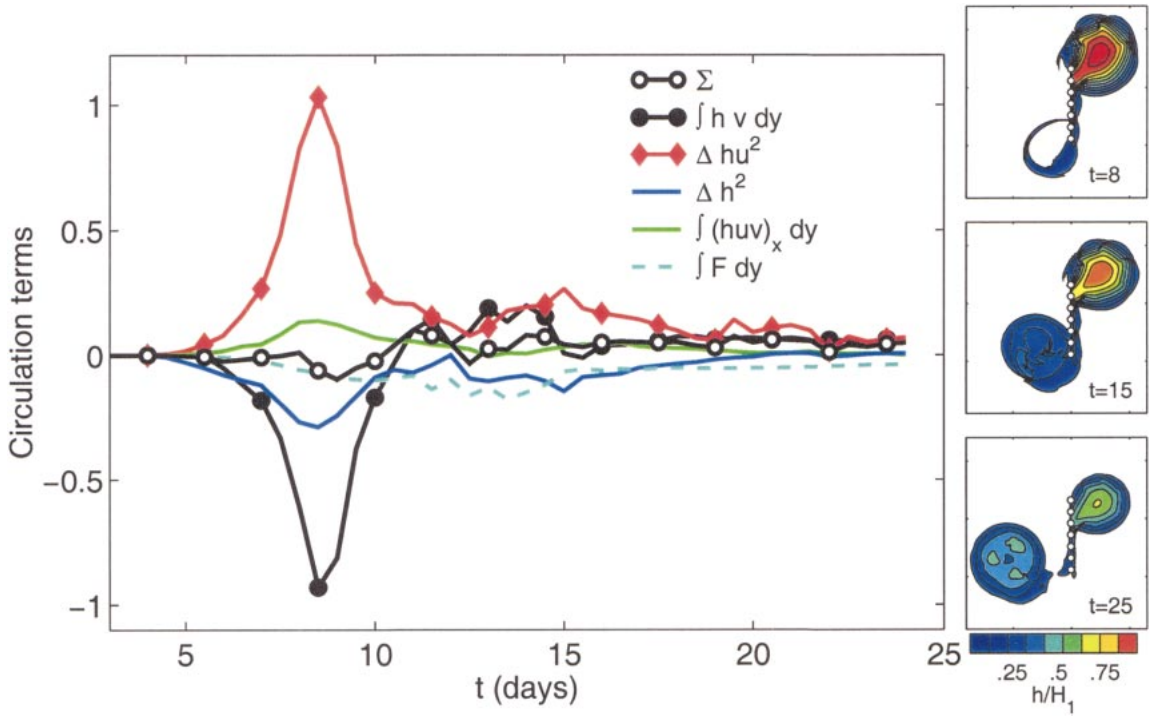

FIG. 15. Diagnosis of the source terms in (19), illustrating the development of circulation resulting from the collision of an intensely nonlinear eddy and a single meridional island. (See section 4e. for the nondimensionalization). Note that friction ($\int \mathbf{F}\, dy$), diagnosed from the model, but not accounted for by (19), cannot be responsible for the generation of the circulation. The symbol Σ represents the sum of the terms in (19) plus the (small) numerical friction term. The total sums nearly to zero, as it should. It is clear that circulation generation ($\partial/\partial t \int h\nu\, dy$) is primarily due to the flow separation at the tips of the walls. Snapshots at various times during the integration are shown in the three panels on the right-hand side of the figure. The location of the wall is indicated by the open circles. Note that for clarity, only every tenth wall point is indicated.

bedded in a viscous medium with continuously varying temperature and salinity, so that even when eddies are observed to have a core in solid body rotation, the outer velocity field decays gradually.

- *Ocean boundaries are not vertical walls, but are continuously shoaling bottoms.* While our geometric simplifications were severe, we considered them necessary as a first approach to the problem. We again justify our simplifications on the grounds that the topographic slope is much greater than the ring interface slope so that effectively the rings ''see'' a vertical wall (Fig. 2). Neglecting topography in the lower layer is also partially justified by the findings of Kamenkovich et al. (1996), who showed that baroclinic lenses crossing a ridge tend to evolve toward a compensated state with a motionless lower layer. Additionally, the near-equatorial ocean is strongly stratified, so that a reduced-gravity model may be appropriate.
- *Our experiments were limited to collisions of zonally translating lenses with meridional walls.* NBCRs probably strike the LA somewhat obliquely and this may explain why some NBCRs are observed to stall and skate to the north of the LA without entering the Caribbean Sea. The obliquity of the collision may be relevant, but is beyond the scope of our study.

7. Summary

We found that the lens propagation rate through a single gap [$(1/12)(\beta R(t)^2$] is identical in principle to the westward drift of an eddy with in an unbounded domain except that in the case of a gap, the radius varies with time. Numerical experiments compared favorably with this theory (Fig. 8).

As with lenses forced by β, *intense* lenses remained axisymmetric as they were advected through the gaps. They were ''stiff'' and hence remained quasi-circular, stalling and draining via wall jets (similar to the β-induced collision shown on the left-hand side of Fig. 7) while the underlying fluid flowed into the western basin (e.g., the upper panel of Fig. 11). On the other hand, *weak* lenses were ''slaves'' to the advective flow (e.g., the right-hand column of Fig. 7, Fig. 10b, or the bottom panel of Fig. 11) and were squeezed through the gap without coming directly into contact with the walls, thereby preventing the formation of wall jets.

Dramatic squeezing of a lens through a gap that is much narrower than the lens initial diameter occurred for parameters that are physically plausible. For example, in experiment 16 (right-hand column of Fig. 7), the speed of the advecting flow through the center of

the gap was 50 cm s^{-1}, the maximum swirl speed of the initial eddy was 80 cm s^{-1}, the initial eddy diameter was 280 km, and the gap width was 80 km. And yet, more than 85% of the lens fluid was forced through a gap that is less than one-third the diameter of the lens. For a gap width and forcing characteristic of the LA, about half of the lens fluid passes through an individual gap (e.g., expts 10 and 12 in Fig. 10). Even individually, the very narrow gaps of the LA do not necessarily constitute a complete barrier to the passage of NBCRs.

When there were multiple gaps, circulation developed around the individual islands (Fig. 15) and *all* the fluid contained in the initial eddy ultimately penetrated into the interior of the western basin. Other significant aspects of the multiple gap numerical experiments are (i) β enhances the wall's tendency to break up the eddy (e.g., Fig. 13, expt 35), (ii) large islands (e.g., $L/R_i = 1.5$) can break an eddy so that the fluid enters the western basin as multiple offspring of reduced size and intensity (e.g., Fig. 13, experiment 60), (iii) the size of the islands rather than the breadth of the individual gaps determines the number of offspring that enter the western basin, and (iv) finite upper layer depth increases the tendency of the lens to break up, so that islands as small as $L/R_i = 0.5$ break up the eddy.

The main conclusions of our study with regard to the penetration of North Brazil Current rings into the Caribbean Sea are

1) Observations indicate that NBCRs are weak (Ro = 0.2–0.4) and large ($L/R_i = 0.5$). Hence, our solutions suggest that they are likely to enter the Caribbean Sea as coherent structures. Small and intense NBCRs, which are less common, are more likely to be broken up. (These size and intensity distinctions have yet to be confirmed or refuted by the observational evidence, which only indicate that some NBCRs do enter the Caribbean Sea.)
2) Collisions with the Grenadines (the single largest barrier to NBCRs) are likely to result in the breakup of the NBCRs regardless of intensity of the lens.
3) Weak NBCRs are slaves to advection and hence can be squeezed through the passages into the Caribbean Sea with the mean flow. On the other hand, strong NBCRs are stiff and hence are more likely to stall at the LA. A northward component of the flow into the Caribbean Sea could therefore cause NBCRs to slide to the north before entering the Caribbean Sea. There is some evidence to support this from drifter observations (Fig. 3), altimeter analysis (Simmons 2000), and OGCMs.

Acknowledgments. Discussions with D. Fratantoni and P. Richardson were very helpful. Drifter data was provided by Richard Limeburner. We wish to acknowledge very useful conversations with J. Pedlosky regarding Kelvin's theorem. The comments of the two anonymous reviewers, particularly the one who suggested that the circulation be discussed in detail, are very much appreciated. This study was supported by the National Aeronautics and Space Administration Earth System Science Fellowship NGT5-30164, the National Science Foundation under Contracts OCE 9503816 and 9633655, National Aeronautics and Space Administration Grants NAGW-4883 and NAG5-7630, and Office of Naval Research Grant N00014-89-J-1606.

APPENDIX

List of Symbols and Terms

H_i	Initial thickness at the center of the eddy.
H_∞	Layer depth at the edge of the eddy.
ε	Ratio of long to short timescales for β-induced collision, $\beta R_d f^{-1}$.
$\mathcal{S}$	Integration area.
U	Velocity of lower layer at center of the gap.
μ	Ratio of long to short timescales for advection-induced collision, $U(f\mathrm{Ro}R_i)^{-1}$.
β	Linear variation of the Coriolis parameter with latitude.
R_i	Initial lens radius.
Ro	Rossby number.
R_d	Rossby radius of deformation, $(g'H)^{1/2} f^{-1}$.
v_θ	Azimuthal component of velocity.
C	Translation speed of coordinate system in x direction.
D	Distance from lens center to wall in the x direction.
W	Gap width.
R_i	Initial lens radius.
f	Coriolis parameter, $(f_0 + \beta_y)$.
h	Upper layer thickness.
h_H,h_D	Thickness of the southern and northern wall jets.
u,v	Velocities in Cartesian coordinates.
A_h	Laplacian friction in numerical model.
$\Delta x,\Delta y$	Grid resolution in numerical model.
g'	Reduced gravity, $(\Delta\rho/\rho)g$.
V_i	Initial lens volume.
ψ	Streamfunction.
q	Mass flux out of eddy carried by the wall jets.

REFERENCES

Barnier, B., T. Reynaud, A. Beckmann, C. Böning, J.-M. Molines, S. Barnard, and Y. Jia, 2001: On the seasonal variability and eddies in the North Brazil current: Insights from model intercomparison experiments. *Progress in Oceanography*, Vol. 48, Pergamon, 195–230.

Bleck, R., and D. Boudra, 1986: Wind-driven spinup in eddy resolving models formulated in isopycnic and isobaric coordinates. *J. Geophys. Res.*, **91,** 7611–7621.

Boyer, D., and P. Davies, 1982: Flow past a right circular cylinder

on a beta plane. *Philos. Trans. Roy. Soc. London,* **A306,** 533–566.

Brown, W. S., W. E. Johns, K. D. Leaman, J. P. McCreary, R. L. Molinari, P. L. Richardson, and C. Rooth, 1992: A western tropical Atlantic experiment (WESTRAX). *Oceanography,* **5,** 73–77.

Bruce, J. G., 1984: Comparison of eddies of the north Brazilian and Somali coasts. *J. Phys. Oceanogr.,* **14,** 825–832.

——, and J. Kerling, 1984: Near equatorial eddies in the North Atlantic. *Geophys. Res. Lett.,* **11,** 779–782.

——, ——, and W. Beatty, 1985: On the North Brazilian eddy field. *Progress in Oceanography,* Vol. 14, Pergamon, 57–63.

Carnevale, G., R. Kloosterziel, and G. van Heijst, 1991: Propagation of barotropic vortices over topography in a rotating tank. *J. Fluid Mech.,* **233,** 119–139.

Carton, J. A., and Y. Chao, 1999: Caribbean Sea eddies inferred from TOPEX/Poseidon altimetry and a 1/6° Atlantic Ocean model simulation. *J. Geophys. Res.,* **104,** 7743–7752.

Cochrane, J. D., F. J. Kelly, and C. R. Olling, 1979: Subthermocline countercurrents in the western equatorial Atlantic Ocean. *J. Phys. Oceanogr.,* **9,** 724–738.

Cushman-Roisin, B., E. P. Chassignet, and B. Tang, 1990: Westward motion of mesoscale eddies. *J. Phys. Oceanogr.,* **20,** 758–768.

Davies, P., 1972: Experiments on Taylor columns in rotating, stratified fluids. *J. Fluid Mech.,* **54,** 691–717.

Didden, N., and F. Schott, 1993: Eddies in the North Brazil current retroflection region observed by Geosat altimetry. *J. Geophys. Res.,* **98,** 20 121–20 131.

Firing, E., and R. C. Beardsley, 1976: The behavior of a barotropic eddy on a beta-plane. *J. Phys. Oceanogr.,* **6,** 57–65.

Fratantoni, D., W. E. Johns, and T. Townsend, 1995: Rings of the North Brazil Current: Their structure and behavior inferred from observations and a numerical simulation. *J. Geophys. Res.,* **100** (C6), 10 633–10 654.

Goni, G., and W. Johns, 2001: A census of North Brazil Current rings observed from T/P altimetry: 1992–1998. *Geophys. Res. Lett.,* **28,** 1–4.

Haidvogel, D., A. Beckmann, R. Lin, and D. Chapman, 1993: Numerical simulation of flow around a tall isolated seamount. Part II: Resonant generation of trapped waves. *J. Phys. Oceanogr.,* **23,** 2373–2391.

Heburn, G. W., T. H. Kinder, J. H. Allen, and H. E. Hurlburt, 1982: A numerical model of eddy generation in the southeastern Caribbean Sea. *The Hydrodynamics of Semi-Enclosed Seas,* J. C. J. Nihoul, Ed., Elsevier Science, 299–328.

Hogg, N., 1973: On the stratified Taylor column. *J. Fluid Mech.,* **58,** 517–537.

Huppert, H., and K. Bryan, 1976: Topographically generated eddies. *Deep-Sea Res.,* **23,** 655–679.

Johns, E., W. D. Wilson, and R. L. Molinari, 1999: Direct observations of velocity and transport in the passages of the Intra-Americas Sea and the Atlantic Ocean, 1984–1996. *J. Geophys. Res.,* **104,** 25 805–25 820.

Johns, W. E., T. N. Lee, F. Schott, R. J. Zantopp, and R. H. Evans, 1990: The North Brazil Current retroflection: Seasonal cycle and variability. *J. Geophys. Res.,* **95,** 22 103–22 120.

Kamenkovich, V. M., Y. P. Leonov, D. A. Nechaev, D. A. Byrne, and A. L. Gordon, 1996: On the influence of bottom topography on the Agulhas eddy. *J. Phys. Oceanogr.,* **26,** 892–912.

Killworth, P., 1983: On the motion of isolated lenses on a beta-plane. *J. Phys. Oceanogr.,* **13,** 368–376.

LaCasce, J. H., 1998: A geostrophic vortex over a slope. *J. Phys. Oceanogr.,* **28,** 2362–2381.

Limeburner, R., R. Beardsley, I. D. Soares, S. J. Lentz, and J. Candela, 1995: Lagrangian flow observations of the Amazon River discharge into the North Atlantic. *J. Geophys. Res.,* **100** (C2), 2401–2415.

Louis, J., B. Petrie, and P. Smith, 1982: Observations of topographic Rossby waves on the continental margin off Nova Scotia. *J. Phys. Oceanogr.,* **12,** 47–55.

McCartney, M. S., 1975: Inertial Taylor columns on a beta plane. *J. Fluid Mech.,* **68,** 71–95.

McWilliams, J. C., 1998: Oceanic general circulation models. *Ocean Modeling and Parameterization,* E. P. Chassignet and J. Verron, Eds., NATO Science Series, Vol. 516, Kluwer Academic, 1–44.

Milne-Thompson, L. M., 1968: *Theoretical Hydrodynamics.* 5th ed. Dover, 743 pp.

Molinari, R. L., M. Spillane, I. Brooks, D. Atwood, and C. Duckett, 1981: Surface currents of the Caribbean Sea as deduced from Lagrangian observations. *J. Geophys. Res.,* **86,** 6537–6542.

Mory, M., M. E. Stern, and R. W. Griffiths, 1987: Coherent baroclinic eddies on a sloping bottom. *J. Fluid Mech.,* **183,** 45–62.

Murphy, S. J., H. E. Hurlburt, and J. J. O'Brien, 1999: The connectivity of eddy variability in the Caribbean Sea, the Gulf of Mexico, and the Atlantic Ocean, *J. Geophys. Res.,* **104,** 1431–1453.

Nof, D., 1981: On the beta-induced movement of isolated baroclinic eddies. *J. Phys. Oceanogr.,* **11,** 1662–1672.

——, 1995a: Choked flows and wind-driven interbasin exchange. *J. Mar. Res.,* **53,** 23–48.

——, 1995b: Choked flows from the Pacific to the Indian Ocean. *J. Phys. Oceanogr.,* **25,** 1369–1383.

——, 1999: Strange encounters of eddies with walls. *J. Mar. Res.,* **57,** 739–761.

——, and T. Pichevin, 1996: The retroflection paradox. *J. Phys. Oceanogr.,* **26,** 2344–2385.

Olson, D., 1991: Rings in the ocean. *Ann. Rev. Earth Planet. Sci.,* **19,** 283–311.

Orlanski, I., 1976: A simple boundary condition for unbounded hyperbolic flows. *J. Comput. Phys.,* **21,** 251–269.

Pauluhn, A., and Y. Chao, 1999: Tracking eddies in the subtropical north-western Atlantic Ocean. *Phys. Chem. Earth,* **A24,** 415–421.

Pedlosky, J., 2000: The transmission of Rossby waves through basin barriers. *J. Phys. Oceanogr.,* **30,** 495–511.

——, and M. Spall, 1999: Rossby normal modes in basins with barriers. *J. Phys. Oceanogr.,* **29,** 2332–2349.

——, L. Pratt, M. Spall, and K. Helfrich, 1997: Circulation around islands and ridges. *J. Mar. Res.,* **55,** 1199–1251.

Richardson, P. L., 1994: Giant eddies of South Atlantic water invade the north. *Oceanus,* **37,** 19–21.

——, G. E. Hufford, R. Limeburner, and W. S. Brown, 1994: North Brazil Current retroflection eddies. *J. Geophys. Res.,* **99** (C3), 5081–5093.

Rintoul, S. R., 1991: South Atlantic interbasin exchange. *J. Geophys. Res.,* **96,** 32 675–32 692.

Ruddick, B., 1987: Anticyclonic lenses in large scale strain and shear. *J. Phys. Oceanogr.,* **17,** 741–749.

Sanson, L. Z., F. Graef, and E. G. Pavia, 1998: Collision of anticyclonic, lens-like eddies with a meridional western boundary. *J. Geophys. Res.,* **103,** 24 881–24 890.

Schmitz, W. J., 1996: On the world ocean circulation: Volume I. Woods Hole Oceanographic Institution Tech. Rep. WHOI-96-03, 150 pp.

——, and P. L. Richardson, 1991: On the sources of the Florida Current. *Deep-Sea Res.,* **38,** S379–S409.

Schott, F., J. Fischer, and L. Stramma, 1998: Transports and pathways of the upper-layer circulation in the western tropical Atlantic. *J. Phys. Oceanogr.,* **28,** 1904–1928.

Sheremet, V. A., 2001: Hysteresis of a western boundary current leaping across a gap. *J. Phys. Oceanogr.,* **31,** 1247–1259.

Simmons, H. L., 2000: The destruction of eddies by gaps and islands. Ph. D. thesis, The Florida State University, 127 pp.

——, and D. Nof, 2000: Islands as eddy splitters. *J. Mar. Res.,* **58,** 919–956.

Smith, D. C., and J. J. O'Brien, 1983: The interaction of a two layer isolated mesoscale eddy with topography. *J. Phys. Oceanogr.,* **13,** 1681–1697.

Smith, W. H. F., and D. T. Sandwell, 1997: Global seafloor topography from satellite altimetry and ship depth soundings. *Science,* **277,** 1956–1962.

Stansfield, K. L., M. J. Bowman, S. J. Fauria, and T. C. Wilson, 1995: Water mass and coastal current variability near Barbados, West Indies. *J. Geophys. Res.*, **100** (C12), 24 819–24 830.

Stern, M., 2000: Scattering of an eddy advected by a current towards a topographic obstacle. *J. Fluid Mech.*, **402,** 211–223.

Swaters, G. E., and G. Flierl, 1991: Dynamics of ventilated coherent cold eddies on a sloping bottom. *J. Fluid Mech.*, **223,** 565–587.

Velasco Fuentes, O. U., and G. F. van Heijst, 1994: Experimental study of dipolar vortices on a topographic β-plane. *J. Fluid Mech.*, **259,** 76–106.

Wilson, W. D., and W. E. Johns, 1997: Velocity structure and transport in the Windward Islands passages. *Deep-Sea Res.*, **44,** 487–520.

Zalesak, S. T., 1979: Fully multidimensional flux-corrected transport algorithms for fluids. *J. Comput. Phys.*, **31,** 335–362.

Zhang, X., and D. L. Boyer, 1991: Current deflections in the vicinity of multiple seamounts. *J. Phys. Oceanogr.*, **21,** 1122–1138.